THE UNIVERSITY OF CHICAGO

DENSITY MATRICES: FROM EXCITONS TO MOLECULES

A DISSERTATION SUBMITTED TO
THE FACULTY OF THE DIVISION OF THE PHYSICAL SCIENCES
IN CANDIDACY FOR THE DEGREE OF
DOCTOR OF PHILOSOPHY

DEPARTMENT OF CHEMISTRY

BY
CHARLES C. FORGY

CHICAGO, ILLINOIS
AUGUST 2017

To Hadas

TABLE OF CONTENTS

LIST OF FIGURES

LIST OF TABLES

ACKNOWLEDGMENTS

It is impossible to fully acknowledge all the people who have made my journey to a PhD possible. First and foremost, I must acknowledge my advisor, David Mazziotti. David has led me every step of the way on my journey, providing guidance and advice far beyond that expected from his position. If I had not been fortunate enough to have an advisor like David, I almost certainly could not have completed my degree.

I must also thank all the post-docs and other graduate students in our group, past and present, for their assistance and support. Srikant, Chad, Andrew, and Eric provided invaluable help in "teaching me the ropes" showing me how use our group's software and systems. Erica, Valentine, Anthony, Romit, Manas, Ali, Kade, Shiva, and Shayan have been a constant source of support and guidance. In particular, I must acknowledge Anthony for his tireless willingness to scoot over his chair to assist with GAMESS and, on occasion, translate papers from German.

My parents have been an unending source of support and encouragement throughout my studies. Furthermore, the technical advice I received from my father in computer science and the general advice about graduate school was always welcome and greatly helpful.

Finally, I must acknowledge my wife Hadas. Without her support at home I never possibly could have undertaken as time- and energy-intensive an endeavor as graduate school. Words fail me here, so all I can say is thank you!

ABSTRACT

The most computationally intensive element of most electronic-structure calculations, be they Hartree-Fock, DFT, coupled-cluster, RDM, or any other method, is calculation of the four-center electron repulsion integrals (ERIs). As the number of four-center integrals formally scale as $\mathcal{O}(n^4)$, even a relatively small system will necessitate the calculations of numerous ERIs. Furthermore, memory and latency concerns make it inadvisable to store all calculated integrals. Instead, integrals are generally calculated as needed, erased, and if needed calculated again, further increasing the number of ERIs calculated. Thus rapid and efficient methods of evaluating ERIs are of great significance in quantum chemistry.

Over the years, numerous ingenious methods have been devised to speed the evaluation of Gaussian ERIs. One of the most successful and widespread of these is the Obara-Saika method, and its associated refinements due largely to Pople and Head-Gordon [21]. Though the relationship between the Obara-Saika method and Schlegel's derivative theorem [53] have long been recognized [26] , no paper to date has elucidated the exact nature of this relationship. Instead, most texts rely on rather obtuse proofs to the Obara-Saika method, essentially postulating the result and then proving it to be correct. In Ch. 2 we present an explicit derivation of the Obara-Saika method, beginning with the definition of Gaussian integrals and Schlegel's derivative theorem, and proceeding to explicitly build the proof from that foundation.

We then shift tracks to discuss the use of density matrices in quantum chemistry. In Ch. 4 we explore the application of density matrices to excitonic transport. In Secs. 1.2.2 & 4.2.2 we introduce the use of a Lindblad master equation, and explain its application to open quantum systems. In particular, we discuss the role of dephasing noise in excitonic transport in one- and two-dimensional systems, and demonstrate how dephasing noise can be beneficial to said transport. We demonstrate that optimal dephasing rates exist, but that while in homogenous systems the optimal dephasing rate is determined by the coupling, whereas in inhomogeneous systems the optimal coupling rate is determined by the topology

of the system.

Recently, experimental verifications of the geometry of the benzene dication [29] and the closely related hexamethylbenzene dications [37] have been achieved. In both cases, the lowest energy geometry is a pentagonal-pyramid with a hexacoordinated carbon. In Ch. 3 we discuss the optimal geometries of the as of yet unstudied nitrobenzene and aniline dications. We demonstrate that the nitrobenzene dication structure is expected to closely resemble the parent benzene dication's structure, while the aniline dication is expected to more closely resemble the neutral aniline structure. In the process, we demonstrate that the results obtained from reduced-density-matrix methods compare favorably with the results of the more expensive coupled-cluster calculations.

CHAPTER 1

INTRODUCTION

1.1 The Schrödinger Equation and Basis Functions in Quantum Chemistry

1.1.1 The Modern Basis of Chemistry

The twin revolutions of twentieth century physics were the discovery of quantum mechanics and relativity. While relativity generally has little bearing on chemistry (expect for heavy element chemistry and/or exceedingly high precision calculations), quantum mechanics forms the basis of most of modern chemistry. In the early days of quantum mechanics, it was recognized that the Schrödinger equation and its wave-function solutions contain all the information necessary to predict all chemical behavior. In 1929 Paul Dirac [16] famously wrote

> The underlying physical laws necessary for the mathematical theory of a large part of physics and the whole of chemistry are thus completely known, and the difficulty is only that the exact application of these laws leads to equations much too complicated to be soluble. It therefore becomes desirable that approximate practical methods of applying quantum mechanics should be developed, which can lead to an explanation of the main features of complex atomic systems without too much computation.

While Dirac was correct–in the non-relativistic limit–in his assertion in the completeness of the laws of chemistry, the development of “approximate practical methods” proved to be a problem that to this day is the source of much effort and original research.

1.1.2 The Schrödinger Equation

The standard formalism of quantum mechanics for a time-independent system is the time-independent Schrödinger equation (TISE)

$$\hat{H}\Psi = E\Psi \tag{1.1}$$

where $\hat{H}$ in an operator consisting of the kinetic and potential energies of all particles in a given system

$$\hat{H} = \sum \frac{-\hbar}{2m_i}\nabla_i^2 + \sum V_i(\mathbf{r_i}) \tag{1.2}$$

where m_i is the mass of particle i and $V_i(\mathbf{r_i})$ is its potential in space experienced from the repulsion and attraction of charged particles, interactions with electric and magnetic fields, etc. Ψ is a function describing all particles in a system, and E is the total energy of the system.

It is thus recognized that 1.1 is an eigenvalue problem, and our goal is discover Ψ, or at least close approximations to it. Knowledge of a close approximation to the true wavefunction Ψ will in turn inform us of not merely the energy, but all observables of the system, such as spectroscopic results.

1.1.3 The Born-Oppenheimer Approximation

While the above is conceptually straightforward, this approach is computationally intractable for any system much more complicated that a single hydrogen atom. One of the earliest developments in furthering quantum chemistry was the Born-Oppenheimer approximation (BOA), first developed by Max Born and J. Robert Oppenheimer in 1927 [5]. In brief, the BOA states that due the extreme differences in mass between an electron and a nucleus (around 2000-fold for hydrogen, and even greater for heavier elements), we may assume that the electronic motion takes place on a scale too rapid to effect an appreciable response from the nuclei. Thus, we may separate the Eq. 1.1 into the sum of the nuclear and electronic Hamiltonians. Introducing $\hat{h}$ for the electronic portion of the Hamiltonian and lower (upper) case indices for electrons (nuclei), we have

$$\hat{H} = \hat{H}_N + \hat{h}, \tag{1.3}$$

$$\hat{H}_N = \sum_I -\frac{1}{2m_I}\nabla_I^2 + \sum_{K>I} \frac{Z_I Z_K}{r_{IK}}, \tag{1.4}$$

and

$$\hat{h} = \sum_j -\frac{1}{2}\nabla_j^2 - \sum_{j,I} \frac{Z_I}{r_{Ij}} + \sum_{l>i} \frac{1}{r_{il}}, \tag{1.5}$$

where we have introduced atomic units in which $m_e = \hbar = e = 4\pi\epsilon_0 = 1$, and Z_I is the nuclear charge.

Using the BOA, we may 'freeze' the nuclei in a given geometry, and then optimize the solution to the electronic Hamiltonian. By primarily concerning ourselves with the electronic portion of the Hamiltonian, we significantly reduce the complexity of chemical calculations.

1.1.4 Boys Functions

We are now left solving

$$\hat{h}\psi = E_e\psi, \tag{1.6}$$

where ψ indicates the electronic portion of the wave-function. E_e is the electronic energy, hereafter referred to simply as the energy.

To solve Eq. 1.6, we must be begin with some guess for ψ to approximate the true wave-function, know as the basis set. The choice of function(s) for the basis set is one of the most fundamental choices in all of quantum chemistry.

As mentioned, the exact (non-relativistic) solution to the hydrogen atom is known. For our purposes, the significant portion of the hydrogenic wave-functions is that they consist of a polynomial multiplied by an exponential. A natural assumption is to use similar functions to solve Eq. 1.6. This was indeed one of the earliest approaches advanced, resulting in the creation of Slater-type orbitals (STOs) of the form

$$Y_{l,m}(\theta, \phi) r^n e^{-\zeta r} \tag{1.7}$$

where $Y_{l,m}$ are the spherical-harmonics, further discussed in Sec. 2.1.1 in Eq. 2.8. While there do exist modern quantum chemistry packages that utilize STOs [6] as basis functions, the vast majority of all packages do not use them.

The reason for the disfavor of STOs stems from the exponential term, $e^{-\zeta r}$. It is impossible to rapidly integrate exponential functions for the computationally intensive integrals discussed in Sec. 2.2. For this reason, in 1950 S. F. Boys [7] introduced the use of gaussian functions of the form $e^{-\alpha r^2}$ instead. Basis functions comprised of gaussians are referred to as Gaussian-type orbitals (GTOs), and will be defined in Sec. 2.1.1.

From a purely physical view, gaussians are inferior to exponentials inasmuch as gaussians remain finite at all points in space, while the electrostatic repulsion between charged particles is infinite for a charge separation of zero. For this reason and others, a gaussian, or a linear combination of a given number gaussians, will give an inferior approximation to the true ψ than the same number of STOs. However, for the complicated integrals that arise in quantum chemistry, particularly those describing intra-electronic repulsion, integrals of GTOs can be solved far more simply and rapidly than integrals of STOs. Furthermore, any given STO can be approximated to arbitrary precision through a linear combination of GTOs [21]. Thus, the fact that a greater number of GTOs than STOs are required to accurately resemble ψ is more than offset by the extreme increase in computational speed achieved through use of GTOs.

While the calculation of integrals of GTOs is simple relative to integrals of STOs, this should not be construed as implying that it is objectively simple. Over the years there have been numerous methods advanced to solve these integrals. Ch. 2 consists of discussion of the Obara-Saika method, one of the most important of these methods. In the process of its discussion, we shall derive a novel and more direct proof to the Obara-Saika method.

1.2 Density Matrices

Up to this point we have discussed pure systems–that is to say a single system that can be described by a single wave-function. However, in the real world we often wish to discuss an *ensemble* of states, be they a group of photons with differing polarizations, a group of particles with differing vibrational and rotational states, or any other collection of objects possessing differing quantum states. Clearly, in general we cannot expect all elements of a system to be described by identical wave-functions. Rather, the system is best understood as a *statistical ensemble* of elements.

This ensemble can be described through a density matrix, ρ. To create ρ, let us assume that the wave-function of each element i can be described by the row vector $|\psi_i\rangle$[1]. Letting $\langle\psi_i|$ represent the transpose column vector, we may then create the matrix

$$\rho_i = |\psi_i\rangle\langle\psi_i|. \tag{1.8}$$

The operation in Eq. 1.8 is known as the 'outer product,' sometimes also referred to as the tensor product.

If the probability of an element of the the system existing in state i is written as p_i, then the entire density matrix may be constructed as

$$\rho = \sum_i p_i|\psi_i\rangle\langle\psi_i| \tag{1.9}$$

---

[1] This formalism can equally well be used to describe wave-functions of the form discussed in Sec. 1.1.4 or wave-functions of any other mathematical function. The chief difference in such a case is that Eq. 1.8 would instead be understood to represent integration.

where

$$\sum_i p_i = 1. \tag{1.10}$$

1.2.1 Time Dependent Schrödinger Equation

In Sec. 1.1.2 we discussed the Schrödinger Equation for systems that do not change with respect to time. For systems that do evolve with time, we must use the more inclusive Time Dependent Schrödinger Equation (TDSE)

$$i\hbar\frac{\partial}{\partial t}\Psi = \hat{H}\Psi \tag{1.11}$$

or, in atomic units and vector notation,

$$i\frac{\partial}{\partial t}|\Psi\rangle = \hat{H}|\Psi\rangle \tag{1.12}$$

where $\hat{H}$ is defined as in Sec.s 1.1.2-1.1.3.

1.2.2 The Liouville-von Neumann Equation

We may now derive the equivalent to Eq. 1.12 for density matrices. Consider Eq. 1.12 and its transpose

$$-i\frac{\partial}{\partial t}\langle\Psi| = \langle\Psi|\hat{H}. \tag{1.13}$$

We may now derive

$$\begin{aligned}
\frac{\partial\rho}{\partial t} &= \frac{\partial}{\partial t}\bigg(|\Psi\rangle\langle\Psi|\bigg) \\
&= \bigg(\frac{\partial}{\partial t}|\Psi\rangle\bigg)\langle\Psi| + |\Psi\rangle\bigg(\frac{\partial}{\partial t}\langle\Psi|\bigg) \\
&= \bigg(-i\hat{H}|\Psi\rangle\bigg)\langle\Psi| + |\Psi\rangle\bigg(i\langle\Psi|\hat{H}\bigg) \\
&= -i\bigg(\hat{H}|\Psi\rangle\langle\Psi| - |\Psi\rangle\langle\Psi|\hat{H}\bigg) \\
&= -i[\hat{H},\rho],
\end{aligned} \tag{1.14}$$

where the notation of $[A,B]$ indicates the commutator of A and B. Eq. 1.14 is know as the Liouville-von Neumann Equation, or the Quantum Liouville Equation.

Up to here, our treatment has been exact. Eq. 1.14 is a rearrangement of the TDSE, and hence will return exact solutions (to the limit of the accuracy of our basis set or vectors). However, at times we may wish to include terms to model the interaction of the environment with an otherwise largely closed system. Though we could simply expand our wave-function to include the environment, this is computationally expensive and often unnecessary.

In many scenarios, the environmental interactions are Markovian ("memoryless"), or loosely speaking unidirectional. That is to say that the environment, or 'bath,' exerts an essentially steady and uniform influence on the system, which causes the system to evolve and change. However, due to the size of the bath and comparatively slow speed at which the bath reacts to influences from the system, the bath–and hence its influence on the system–remains essentially unchanged during the time-frame of interest.

In such situations, we introduce a Lindblad operator. The Linblad operator, $\hat{L}$, is defined as

$$\begin{aligned}
\hat{L}_i(\rho) &= 2L_i\rho L_i^\dagger - L_iL_i^\dagger\rho - \rho L_iL_i^\dagger \\
&= 2L_i\rho L_i^\dagger - \{L_iL_i^\dagger,\rho\},
\end{aligned} \tag{1.15}$$

where we have introduced the anti-commutator, $\{A, B\}$. We may now present the Lindblad master equation

$$\frac{\partial \rho}{\partial t} = -i[\hat{H}, \rho] + \sum_i \hat{L}_i(\rho). \tag{1.16}$$

While the derivation of the Linbald master equation will not be presented here (see, for example, Ref. [45]), the Linblad operator can be understood heuristically as introducing a 'drag' term to the Liouville-von Neumann Equation. The two most salient features of Eq. 1.16 are that is (a) non-unitary, i.e. it allows density to be added to or removed from the system; and (b) Hermitian, hence ensuring that the evolution of the system remains in the space of observables.

The application of the Linbald master equation to excitonic transport in various systems of varying topology and homogeneity will be explore in Ch. 4.

1.2.3 Reduced Density Matrices

The density-matrix formalism may also be used to solve standard electronic-structure calculations, with Eq. 1.8 understood as referring to integration. The central point of this formulation is the observation that electrons interact only in a pairwise fashion [38]. As all electrons are indistinguishable, it is possible to calculate the energy of any molecular system as a functional of the two-electron reduced density matrix (2-RDM)

$$^2\mathbf{D}(1, 2; 1'2') = \int \Psi(1, 2, \ldots, N)\Psi(1', 2', \ldots, N) d3 \ldots dN. \tag{1.17}$$

Early attempts to utilize the 2-RDM resulted in energies lower than the true ground-state energy, failing to obey the Rayleigh-Ritz variational principle [60, 13]. This was shown to be a result of the fact that the space of 2-RDMs is larger than the space of possible wavefunctions. To address this shortcoming it was necessary to develop what are now referred to as *N-representability conditions* [40].

Briefly, the N-representability conditions ensure that RDMs remain physical by possessing non-negative probabilities of describing either (a) two electrons in two orbitals, (b) two holes (i.e. no electrons) in two orbitals, or (c) one electron and one hole in two orbitals. When the 2-RDMs are parameterized according to these conditions, we achieve a density-matrix method of calculating electronic-structure known as *p2-RDM*. Studies by Mazziotti have demonstrated that p2-RDM calculations compare favorably to more expensive methods, such as coupled-cluster methods [15]. Ch. 3 discusses the the application of p2-RDM methods to the benzene dication and related structures, and contrasts the results with results obtained through coupled-cluster calculations.

CHAPTER 2

A SIMPLE DERIVATION OF SCHLEGEL'S DERIVATIVE THEOREM AND THE OBARA-SAIKA METHOD

2.1 Introduction

2.1.1 Types of Gaussian Orbitals

There are three major types of Gaussian basis functions in common use in electronic structure calculations–either as basis functions in their own right or intermediates in calculations.

(a) Cartesian Gaussians (CG) are defined as

$$\phi_C(\mathbf{r}, \alpha, \mathbf{A}, n_{A_x}, n_{A_y}, n_{A_z}) = N(x - A_x)^{n_{Ax}}(y - A_y)^{n_{Ay}}(z - A_z)^{n_{Az}} e^{-\alpha(\mathbf{r}-\mathbf{A})^2} \tag{2.1}$$

for normalization constant N, exponential coefficient α, and nuclear coordinate vector $\mathbf{A}$, and where $(\mathbf{r} - \mathbf{A})^2 = (x - A_x)^2 + (y - A_y)^2 + (z - A_z)^2$. CGs are defined in terms of their total angular momentum number $n = n_{A_x} + n_{A_y} + n_{A_z}$. Thus the $n = 0$ CG is the s-type orbital, the three $n = 1$ CGs are p-type orbitals, and so on.

CGs obey the identities

$$\begin{aligned} &\frac{\partial}{\partial A_x}\phi_C(\mathbf{r}, \alpha, \mathbf{A}, n_{A_x}, n_{A_y}, n_{A_z}) \\ &= 2\alpha\phi_C(\mathbf{r}, \alpha, \mathbf{A}, n_{A_x} + 1, n_{A_y}, n_{A_z}) - n_{A_x}\phi_C(\mathbf{r}, \alpha, \mathbf{A}, n_{A_x} - 1, n_{A_y}, n_{A_z}), \end{aligned} \tag{2.2}$$

and

$$\begin{aligned} &(-1)^n\frac{\partial^n}{\partial\alpha^n}\phi_C(\mathbf{r}, \alpha, \mathbf{A}, n_{A_x}, n_{A_y}, n_{A_z}) \\ &= \phi_C(\mathbf{r}, \alpha, \mathbf{A}, n_{A_x} + 2n, n_{A_y}, n_{A_z}) + \phi_C(\mathbf{r}, \alpha, \mathbf{A}, n_{A_x}, n_{A_y} + 2n, n_{A_z}) \\ &+ \phi_C(\mathbf{r}, \alpha, \mathbf{A}, n_{A_x}, n_{A_y}, n_{A_z} + 2n). \end{aligned} \tag{2.3}$$

We can also consider the relation in Eq. 2.3 as

$$(-1)^n \frac{\partial^n}{\partial \alpha^n} \phi_C(\mathbf{r}, \alpha, \mathbf{A}, 0, 0, 0) = r^{2n} \phi_C(\mathbf{r}, \alpha, \mathbf{A}, 0, 0, 0), \tag{2.4}$$

which among other uses provides a simple method of creating higher level s-orbitals from the linear combination $x^{2n} + y^{2n} + z^{2n}$.

(b) Hermite Gaussians (HG) are defined through the differential relation

$$\phi_H(\mathbf{r}, \alpha, \mathbf{A}, n_{A_x}, n_{A_y}, n_{A_z}) = N \frac{1}{(2\alpha)^n} \frac{\partial^{n_{A_x}}}{\partial A_x^{n_{A_x}}} \frac{\partial^{n_{A_y}}}{\partial A_y^{n_{A_y}}} \frac{\partial^{n_{A_z}}}{\partial A_z^{n_{A_z}}} e^{-\alpha(\mathbf{r}-\mathbf{A})^2}. \tag{2.5}$$

(Generally speaking, the $\frac{1}{(2\alpha)^n}$ term in Eq. 2.5 is included in the normalization constant. We write it explicitly as we shall make use of it in our derivations.) HGs obey the trivial identity

$$\frac{\partial}{\partial A_x} \phi_H(\mathbf{r}, \alpha, \mathbf{A}, n_{A_x}, n_{A_y}, n_{A_z}) = 2\alpha\, \phi_H(\mathbf{r}, \alpha, \mathbf{A}, n_{A_x} + 1, n_{A_y}, n_{A_z}). \tag{2.6}$$

Like with CGs, HGs are grouped into s-type, p-type, etc., based on total angular momentum.

(c) Solid Harmonic Gaussians (SHG) are defined as

$$\phi_S(\mathbf{r}, \alpha, \mathbf{A}, l, m) = N S_{l,m} e^{-\alpha(\mathbf{r}-\mathbf{A})^2} \tag{2.7}$$

where $S_{l,m}$ is a real solid harmonic defined from the real part of the spherical harmonic solutions to Laplace's Equation

$$\nabla^2 \phi = 0. \tag{2.8}$$

Although SHGs (and the extremely closely related spherical harmonic Gaussians) are often used as basis functions, we shall only derive integrals in terms of CGs and HGs. When SHGs are used as a basis set, it will be necessary to use transformations such as those given in Schlegel and Frisch [54] or Reine et al. [49] to obtain the final results. Note that Eq. 2.4

provides a simple method of deriving the r^{2n} terms used in SHGs.

Finally, we note that the s- and p-type ($n = 0, 1$ or $l = 0, 1$) Gaussians are identical for CGs, HGs, and SHGs.

2.2 Background

2.2.1 The Electron Repulsion Integral

The most computationally expensive (and hence rate limiting) step of electronic-structure calculations is the calculation of the repulsive forces between different electrons. This calculation involves gaussians centered on up to four separate coordinates, and integration over two spatial variables. This integral is known as the Electron Repulsion Integral (ERI), and its solutions will occupy the remainder of this chapter [58, 27].

Let the $(ss|ss)$ ERI be represented as

$$\begin{aligned}&(\phi(\mathbf{r},\alpha,\mathbf{A},0,0,0)\phi(\mathbf{r},\beta,\mathbf{B},0,0,0)|\phi(\mathbf{r}',\gamma,\mathbf{C},0,0,0)\phi(\mathbf{r}',\delta,\mathbf{D}),0,0,0)\\&=\int\int N\frac{e^{-\alpha(\mathbf{r}-\mathbf{A})^2}e^{-\alpha(\mathbf{r}-\mathbf{B})^2}e^{-\alpha(\mathbf{r}'-\mathbf{C})^2}e^{-\alpha(\mathbf{r}'-\mathbf{D})^2}}{|\mathbf{r}-\mathbf{r}'|}d\mathbf{r}d\mathbf{r}'.\end{aligned}\tag{2.9}$$

To simplify the notation, we may also represent Eq. 2.9 simply as

$$(\mathbf{AB}|\mathbf{CD}).\tag{2.10}$$

Where it is necessary to specify whether an ERI is in a HG or CG basis, we shall use the notation $(\mathbf{AB}|\mathbf{CD})^H$ or $(\mathbf{AB}|\mathbf{CD})^C$, respectively.

The derivation of the solution to Eq. 2.9 can be found in numerous sources (in particular see [22] and [27]), and need not be reproduced for our purposes. Instead, we simply present the final result:

The zeroth order Boys function is defined as

$$F_0(T) = \frac{\operatorname{erf}\sqrt{T}}{\sqrt{T}}, \tag{2.11}$$

while higher order Boys functions can be obtained via differentiation

$$F_n(T) = (-1)^n \frac{d^n}{dT^n} F_0(T). \tag{2.12}$$

The arguments of the functions are as follows:

$$u = -\frac{\alpha\beta}{\alpha+\beta}(\mathbf{A}-\mathbf{B})^2 - \frac{\gamma\delta}{\gamma+\delta}(\mathbf{C}-\mathbf{D})^2, \tag{2.13}$$

and

$$T = \frac{(\alpha+\beta)(\gamma+\delta)}{\alpha+\beta+\gamma+\delta} \sum_{i=x,y,z} \left(\frac{\alpha A_i + \beta B_i}{\alpha+\beta} - \frac{\gamma C_i + \delta D_i}{\gamma+\delta} \right)^2. \tag{2.14}$$

Finally, the normalization constant for the target (Cartesian) integral can be expressed as:

$$\begin{aligned} &N(\alpha,\beta,\gamma,\delta,n_{A_x},n_{A_y},\ldots,n_{D_z}) = \\ &8\frac{\alpha^{\frac{1}{2}(n_{A_x}+n_{A_y}+n_{A_z}+\frac{3}{2})}\beta^{\frac{1}{2}(n_{B_x}+n_{B_y}+n_{B_z}+\frac{3}{2})}\gamma^{\frac{1}{2}(n_{C_x}+n_{C_y}+n_{C_z}+\frac{3}{2})}\delta^{\frac{1}{2}(n_{D_x}+n_{D_y}+n_{D_z}+\frac{3}{2})}}{(\alpha+\beta)(\gamma+\delta)\sqrt{\alpha+\beta+\gamma+\delta}} \\ &\times \sum_{i=n_{A_x},n_{A_y},\ldots,n_{D_z}} \frac{2^i}{\sqrt{(2i-1)!!}}. \end{aligned} \tag{2.15}$$

Where, as above, n_{A_x} is the angular momentum in the x coordinate of the orbital on center $\mathbf{A}$, and the other terms are interpreted analogously.

Using this notation, the integrated form of Eq. 2.9 is expressed as

$$N(\alpha, \beta, \gamma, \delta, 0, 0, \ldots, 0)K(u)F_0(T). \tag{2.16}$$

As Eq. 2.9 involves up to four distinct orbitals, the number of integrals in a given electronic-structure calculations formally scales as $\mathcal{O}(n^4)$, where n is the number of orbitals in the atom or molecule under consideration. However, for a large molecule the interactions between orbitals separated by a large distance will be negligible. In such situations we may apply *integral screening* to remove inconsequential integrals before evaluation. For very large systems, the total number of retained ERIs after integral screening approaches $\mathcal{O}(n^2)$ [27].

2.2.2 Obara-Saika Method

Arguably the single most important development in the evaluation of ERIs was the recognition that ERIs composed of Gaussian orbitals of higher angular momentum may be related to those of lower angular momentum. This allows the calculation of all necessary ERIs to be performed as the all s-type integral of Eq. 2.9 exclusively. Various recurrence-relations may then be applied to transform $(ss|ss) \rightarrow (p_i s|ss)$, $(p_i s|ss) \rightarrow (p_i p_j|ss)$, and so on up to the target integral.

In Obara and Saika's orginal 1986 paper [44], an eight term vertical recurrence relation (VRR) was presented for CGs. Letting $a = n_{A_i}$, $b = n_{B_i}$, etc., the Obara-Saika VRR

(OS-VRR) may be represented as

$$
\begin{aligned}
&(\mathbf{A}_{i,a}\mathbf{B}_{i,b}|\mathbf{C}_{i,c}\mathbf{D}_{i,d+1})^{m} = (C_i - D_i)\frac{\gamma}{\gamma+\delta}(\mathbf{A}_{i,a}\mathbf{B}_{i,b}|\mathbf{C}_{i,c}\mathbf{D}_{i,d})^{m} \\
&+ \frac{\alpha+\beta}{\alpha+\beta+\gamma+\delta}\left(\frac{\alpha A_i + \beta B_i}{\alpha+\beta} - \frac{\gamma C_i + \delta D_i}{\gamma+\delta}\right)(\mathbf{A}_{i,a}\mathbf{B}_{i,b}|\mathbf{C}_{i,c}\mathbf{D}_{i,d})^{m+1} \\
&+ \frac{d}{2(\gamma+\delta)}\left((\mathbf{A}_{i,a}\mathbf{B}_{i,b}|\mathbf{C}_{i,c}\mathbf{D}_{i,d-1})^{m} - \frac{\alpha+\beta}{\alpha+\beta+\gamma+\delta}(\mathbf{A}_{i,a}\mathbf{B}_{i,b}|\mathbf{C}_{i,c}\mathbf{D}_{i,d-1})^{m+1}\right) \\
&+ \frac{c}{2(\gamma+\delta)}\left((\mathbf{A}_{i,a}\mathbf{B}_{i,b}|\mathbf{C}_{i,c-1}\mathbf{D}_{i,d})^{m} - \frac{\alpha+\beta}{\alpha+\beta+\gamma+\delta}(\mathbf{A}_{i,a}\mathbf{B}_{i,b}|\mathbf{C}_{i,c-1}\mathbf{D}_{i,d})^{m+1}\right) \\
&+ \frac{a}{2(\alpha+\beta+\gamma+\delta)}(\mathbf{A}_{i,a-1}\mathbf{B}_{i,b}|\mathbf{C}_{i,c}\mathbf{D}_{i,d})^{m+1} \\
&+ \frac{b}{2(\alpha+\beta+\gamma+\delta)}(\mathbf{A}_{i,a}\mathbf{B}_{i,b-1}|\mathbf{C}_{i,c}\mathbf{D}_{i,d})^{m+1}
\end{aligned}
\tag{2.17}
$$

where the j and k angular momentum values remain constant through all terms. The m superscripts relate to the order in the Boys function of the integral; m implies that the Boys function is of the order expected for the given integral (0 for $(ss|ss)$, 1 for $(p_i s|ss)$, 2 for $(p_i p_j|ss)$, and so on), while $m+i$ increases the Boys function order by i. The original derivation presented in Ref. [44] relies on a lengthly and somewhat roundabout connection between overlap integrals and ERIs, and will not be reproduced here.

Finally, it is important to note that the terms in Eq. 2.17 do not increase beyond the given eight for any arbitrary angular momentum–though for lower angular momentum integrals the number of non-zero terms may be fewer then eight.

2.3 Current Derivation

2.3.1 Differential Operators

Our method is predicated upon breaking down the Gaussian ERIs into the two functions previously defined in Eq.s 2.11-2.14, $K(u)$ and $F_n(T)$, and their derivatives. K is the exponential function, i.e. e^u, and $F_n(T)$ is the n-th order Boys function.

Eq.s 2.2 and 2.6 allow us to relate higher order Gaussians to the derivatives of lower order ones with respect to the nuclear coordinates. Note that Eq. 2.9 is integrated with respect to $\mathbf{r}$ and $\mathbf{r}'$. Thus differentiation of Eq. 2.9 with respect to the nuclear coordinates may be applied to the integrated form in Eq. 2.16. This allows for a conceptually simple method of relating solutions to ERIs of Gaussians possessing higher angular momentum to Eq. 2.16, as suggested by Boys in his original paper [7] on Gaussian basis sets and utilized by Obara and Saika for overlap integrals [44].

Top explore this method of solving ERIs, we begin by defining a transformation operator to operate on Eq. 2.16, $\hat{C}(n, \alpha, A_i)$. The operator will represent the ERI's member Cartesian Gaussian of order n as a linear combination of Hermite Gaussian functions up to order n

$$\hat{C}(n, \alpha, A_i) = \begin{cases} \frac{n!}{2^n} \sum_{k=0}^{\frac{n}{2}} \frac{1}{(\frac{n}{2}-k)!\ (2k)!} \frac{1}{\alpha^{\frac{n}{2}+k}} \frac{\partial^{2k}}{\partial A_i^{2k}}, & \text{n even} \\ \frac{n!}{2^n} \sum_{k=0}^{\frac{n-1}{2}} \frac{1}{(\frac{n}{2}-k-\frac{1}{2})!\ (2k+1)!} \frac{1}{\alpha^{\frac{n}{2}+k+\frac{1}{2}}} \frac{\partial^{2k+1}}{\partial A_i^{2k+1}}. & \text{n odd} \end{cases} \tag{2.18}$$

Eq. 2.18 can be derived for any given n through iterative use of a rearranged form of Eq. 2.2. This rearrangement is expressed in operator notation as:

$$\hat{C}(n+1, \alpha, A_i) = \frac{1}{2\alpha} \left(n\ \hat{C}(n-1, \alpha, A_i) + \frac{\partial}{\partial A_i} \hat{C}(n, \alpha, A_i) \right), \tag{2.19}$$

where $\hat{C}(-1, \alpha, A_i) = 0$ and $\hat{C}(0, \alpha, A_i) = \hat{1}$.

In certain cases, we may find it more convenient to refer to all integrals of a certain angular momentum level on a given center, such as $(d_{ij}s|ss)$ or $(f_{ijk}s|ss)$. To do so, let us first define the expanded Kronecker delta function, $\delta_{i_1,i_2,\ldots,i_m}$, to operate on the set $\{i_1, i_2, \ldots, i_m\}$, where m is an even integer:

$$\delta_{i_1,i_2,\ldots,i_m} = \delta_{i_1,i_2} \ldots \delta_{i_{m-1},i_m} + \delta_{i_1,i_3} \ldots \delta_{i_{m-1},i_m} + \cdots + \delta_{i_1,i_m} \ldots \delta_{i_2,i_{m-1}}, \text{m even}, \tag{2.20}$$

where $\delta_{i_1,i_2,\ldots,i_m}$ contains the $\frac{1}{(m/2)!}\frac{m!}{2^{m/2}}$ 2-member partitions of $\{i_1, i_s, \ldots, i_m\}$. Note that for $m = 0$ (the null set), Eq. 2.20 is defined as 1, while for $m = 2$ Eq. 2.20 collapses to the standard Kronecker delta function. Using Eq. 2.20 we may recast Eq. 2.18 as

$$\hat{B}(n_{A_x}, n_{A_y}, n_{A_z}, \alpha, A) =$$
$$\begin{cases} \sum_{k=0}^{\frac{n}{2}} \frac{1}{(2\alpha)^{\frac{n}{2}+k}} \sum_{t,u,v,w\in S}^{Q} \left((\delta_{i_1=t,\ldots,i_{n-2k}=u}) \frac{\partial^{2k}}{\prod_{v,w\neq t,u} \partial A_v \partial A_w} \right), & \text{n even} \\ \sum_{k=0}^{\frac{n-1}{2}} \frac{1}{(2\alpha)^{\frac{n}{2}+k+\frac{1}{2}}} \sum_{t,u,v\in S}^{Q} \left((\delta_{i_1=t,\ldots,i_{n-2k-1}=u}) \frac{\partial^{2k+1}}{\prod_{v\neq t,u} \partial A_v} \right), & \text{n odd} \end{cases} \tag{2.21}$$

where $n = n_{A_x} + n_{A_y} + n_{A_z}$, S is the set of n_{A_x} x's, n_{A_y} y's, and n_{A_z} z's, and Q is the number of distinct partitions of S into $2n-k$ $(2n-k-1)$ expanded Kronecker delta functions multiplied by a derivative of order $2k$ $(2k+1)$.

Finally, for any set of CGs $\{x^{2n}, y^{2n}, z^{2n}\}$ $(\{x^{2n+1}, y^{2n+1}, z^{2n+1}\})$ it is only necessary to apply Eq. 2.18 to create two of the three terms. Eq. 2.3 and 2.4 can then be used as

$$\hat{C}(2n, \alpha, A_k) = (-1)^n \frac{\partial^n}{\partial \alpha^n} - \hat{C}(2n, \alpha, A_i) - \hat{C}(2n, \alpha, A_j). \tag{2.22}$$

or

$$\begin{aligned} \hat{C}(2n+1, \alpha, A_k) = &\Big(\hat{C}(1, \alpha, A_i) + \hat{C}(1, \alpha, A_j) + \hat{C}(1, \alpha, A_k)\Big)(-1)^n \frac{\partial^n}{\partial \alpha^n} \\ &- \hat{C}(2n+1, \alpha, A_i) - \hat{C}(2n+1, \alpha, A_j). \end{aligned} \tag{2.23}$$

This form can offer computational savings as $\hat{C}(2n, \alpha, A_k)$ $(\hat{C}(2n+1, \alpha, A_k))$ requires the computation of a linear combination of derivatives of up to order $2n$ $(2n+1)$, while the $\frac{\partial^n}{\partial \alpha^n}$ term only requires the computation of derivates of order n $(n+1)$.

2.3.2 Definitions of Derivatives

We present a lemma that will be necessary later in the chapter.

Lemma 1. For any function $f(A_x)$ such that f is linear with respect to A_x, and any Gaussian ϕ where ϕ is a CG, HG, or SHG, the following holds:

$$\begin{aligned}
&\frac{\partial^{n_{A_x}}}{\partial A_x^{n_{A_x}}}\Big(f(A_x)\phi(\mathbf{r},\alpha,\mathbf{A},0,n_{A_y},n_{A_z})\Big)\\
&= n_{A_x}\frac{\partial f(A_x)}{\partial A_x}\frac{\partial^{n_{A_x}-1}}{\partial A_x^{n_{A_x}-1}}\phi(\mathbf{r},\alpha,\mathbf{A},0,n_{A_y},n_{A_z}) + f(A_x)\frac{\partial^{n_{A_x}}}{\partial A_x^{n_{A_x}}}\phi(\mathbf{r},\alpha,\mathbf{A},0,n_{A_y},n_{A_z})
\end{aligned} \tag{2.24}$$

Proof. This follows directly from the Leibniz rule

$$\begin{aligned}
&\frac{\partial^{n_{A_x}}}{\partial A_x^{n_{A_x}}}\Big(f(A_x)\phi(\mathbf{r},\alpha,\mathbf{A},0,n_{A_y},n_{A_z})\Big) = \sum_{k=0}^{n_{A_x}}\binom{n_{A_x}}{k}\frac{\partial^k f(A_i)}{\partial A_x^k}\frac{\partial^{n_{A_x}-k}\phi(\mathbf{r},\alpha,\mathbf{A},0,n_{A_y},n_{A_z})}{\partial A_x^{n_{A_x}-k}}\\
&= \binom{n_{A_x}}{n_{A_x}-1}\frac{\partial f(A_x)}{\partial A_x}\frac{\partial^{n_{A_x}-1}}{\partial A_x^{n_{A_x}-1}}\phi(\mathbf{r},\alpha,\mathbf{A},0,n_{A_y},n_{A_z})\\
&+ \binom{n_{A_x}}{n_{A_x}}f(A_x)\frac{\partial^{n_{A_x}}}{\partial A_x^{n_{A_x}}}\phi(\mathbf{r},\alpha,\mathbf{A},0,n_{A_y},n_{A_z})\\
&= n_{A_x}\frac{\partial f(A_x)}{\partial A_x}\frac{\partial^{n_{A_x}-1}}{\partial A_x^{n_{A_x}-1}}\phi(\mathbf{r},\alpha,\mathbf{A},0,n_{A_y},n_{A_z}) + f(A_x)\frac{\partial^{n_{A_x}}}{\partial A_x^{n_{A_x}}}\phi(\mathbf{r},\alpha,\mathbf{A},0,n_{A_y},n_{A_z}),
\end{aligned} \tag{2.25}$$

where the simplification in the last two lines results from the linear nature of $f(A_x)$. Should ϕ be a HG, the identity

$$\begin{aligned}
&\frac{\partial^{n_{A_x}}}{\partial A_x^{n_{A_x}}}\Big(f(A_x)\phi_H(\mathbf{r},\alpha,\mathbf{A},0,n_{A_y},n_{A_z})\Big)\\
&= \frac{n_{A_x}}{2\alpha}\frac{\partial f(A_x)}{\partial A_x}\phi_H(\mathbf{r},\alpha,\mathbf{A},n_{A_x}-1,n_{A_y},n_{A_z}) + f(A_x)\phi_H(\mathbf{r},\alpha,\mathbf{A},n_{A_x},n_{A_y},n_{A_z})
\end{aligned} \tag{2.26}$$

follows immediately from the definition of HGs in Eq. 2.5.

u and T are quadratic with respect to the coordinates, resulting in linear first derivatives, constant second derivatives, and no higher order derivatives. Hence we can represent all necessary derivatives as two first derivative vectors and two second derivative matrices. Further, the second derivative matrices are rather sparse, as only terms of the same coordinate direction (x, y, or z) can be non-zero. Briefly, the non-zero derivatives are as follows:

$$u_{A_i} = -u_{B_i} = -2(A_i - B_i)\frac{\alpha\beta}{\alpha+\beta}, \tag{2.27}$$

$$u_{C_i} = -u_{D_i} = -2(C_i - D_i)\frac{\gamma\delta}{\gamma+\delta}, \tag{2.28}$$

$$u_{A_i,A_j} = u_{B_i,B_j} = -u_{A_i,B_j} = \delta_{i,j}\frac{-2\alpha\beta}{\alpha\ +\ \beta}, \tag{2.29}$$

$$u_{C_i,C_j} = u_{D_i,D_j} = -u_{C_i,D_j} = \delta_{i,j}\frac{-2\gamma\delta}{\gamma\ +\ \delta}, \tag{2.30}$$

$$\begin{aligned}\frac{1}{\alpha(\gamma+\delta)}T_{A_i} = \frac{1}{\beta(\gamma+\delta)}T_{B_i} = \frac{-1}{\gamma(\alpha+\beta)}T_{C_i} = \frac{-1}{\delta(\alpha+\beta)}T_{D_i} \\ = \frac{2}{\alpha+\beta+\gamma+\delta}\left(\frac{\alpha A_i + \beta B_i}{\alpha+\beta} - \frac{\gamma C_i + \delta D_i}{\gamma+\delta}\right),\end{aligned} \tag{2.31}$$

$$\frac{1}{\alpha^2}T_{A_i,A_j} = \frac{1}{\beta^2}T_{B_i,B_j} = \frac{1}{\alpha\beta}T_{A_i,B_j} = \delta_{i,j}\frac{2(\gamma+\delta)}{(\alpha+\beta)(\alpha+\beta+\gamma+\delta)}, \tag{2.32}$$

$$\frac{1}{\gamma^2}T_{C_i,C_j} = \frac{1}{\delta^2}T_{D_i,D_j} = \frac{1}{\gamma\delta}T_{C_i,D_j} = \delta_{i,j}\frac{2(\alpha+\beta)}{(\gamma+\delta)(\alpha+\beta+\gamma+\delta)}, \tag{2.33}$$

and

$$\frac{1}{\alpha\gamma}T_{A_i,C_j} = \frac{1}{\alpha\delta}T_{A_i,D_j} = \frac{1}{\beta\gamma}T_{B_i,C_j} = \frac{1}{\beta\delta}T_{B_i,D_j} = \delta_{i,j}\frac{-2}{\alpha+\beta+\gamma+\delta}, \tag{2.34}$$

where u_{A_i} and T_{A_i} refer to the first derivatives of T and u with respect to A_i, and the other terms are explained analogously.

2.3.3 Structure and Scaling

In the most naïve implementation of our scheme, one could follow Boys [7] and simply apply Eq. 2.18 or Eq. 2.21 to Eq. 2.16, with N replaced by the appropriate normalization constant. The result will be different combinations of elements from the above mentioned vectors and matrices summed and multiplied by each-other and the Boys functions. Using this method allows the calculation of the L-shell [1] at a cost of around 5,000 FLOPs. This value is somewhat higher than other methods, but is still quite reasonable for modern computer architecture.

However, beyond the L-shell the number of FLOPs rapidly becomes unmanageable. To understand the reason for this, we must understand how the differential scaling works. The scaling consists of the product of the following two rules:

(1) The General Leibniz rule: The multivariate n-th differential of a product of two functions has up to 2^n elements–the sum of all binomial coefficients $\sum_k \binom{n}{k}$. This is the result of application of the multivariate Leibniz (or product) rule to the product of $K(u)$ and $F_0(T)$, resulting in

$$\frac{\partial^n}{\partial A_1, \partial A_2, \ldots, \partial A_n} K(u) F_0(T) = \sum_S \frac{\partial^{|S|} K(u)}{\Pi_{i \in S} \partial A_i} \frac{\partial^{n-|S|} F_0(T)}{\Pi_{j \notin S} \partial A_j} \tag{2.35}$$

where S runs over the 2^n subsets of $\{A_1, A_2, \ldots, A_n\}$, and $|S|$ denotes the cardinality of the set S. If all A_i's are identical, Eq. 2.35 collapses to the familiar univariate Leibniz rule, namely

$$\frac{\partial^n}{\partial A_i^n} K(u) F_0(T) = \sum_{k=0}^{n} \binom{n}{k} \frac{\partial^k K(u)}{\partial A_i^k} \frac{\partial^{n-k} F_0(T)}{\partial A_i^{n-k}}. \tag{2.36}$$

Most integrals in the d-shell and higher will have fewer than 2^n elements as not all A_i's will be distinct. However, as there are 12 coordinates, every shell through the $(ff|ff)$ shell contains sufficient A_i's to contain at least one term with n distinct derivatives.

(2) Faà di Bruno's formula: In Eq.s 2.35 and 2.36, nothing further need be done to differentiate $K(u)$. However, differentiating $F_0(T)$ requires the use of the multivariate chain rule. This is most easily expressed using Faà di Bruno's formula, as follows:

---

[1] The L-shell, also referred to as the $(sp)^4$-shell, consists of the 256 integrals containing s- and/or p-type orbitals.

$$\frac{\partial^n}{\partial A_1, \partial A_2, \ldots, \partial A_n} F_0(T) = \sum_S (-1)^{|S|} F_{|S|}(T) \cdot \prod_{Q \in S_1, S_2} \frac{\partial^{|Q|} T}{\Pi_{j \in Q} \partial A_j}, \qquad n > 0 \tag{2.37}$$

where, as above, S runs over all subsets of $\{A_1, A_2, \ldots, A_n\}$. Here, $Q \in S_1, S_2$ denotes that Q only consists of the 1- and 2-element partitions of the set S–the right hand side of Eq. 2.37 will be zero for any subset S which cannot be further partitioned into $|S|$ 1- and/or 2-element subsets. This is a result of the quadratic nature of T in Eq. 2.14.

Faà di Bruno's formula scales according to the Bell polynomials [2]. Although the Bell polynomials lack a clear asymptotic scaling, we have found that the n-th incomplete Bell polynomial can be very well modeled as scaling according to $0.05e^{1.3n} \approx \mathcal{O}(e^n)$ in the range relevant to this work.

Thus the individual integrals will scale as the product of the General Leibniz rule and Faà di Bruno's formula, with the most difficult integrals in a given shell scaling as $2^n 0.05e^{1.3n} \approx \mathcal{O}(e^n)$, where n is four times the value of the highest angular momentum orbital in the shell.

2.3.4 Recurrence Relations

Instead, let us explore methods of reusing values from lower angular momentum integrals to evaluate higher order ones. Using the differential structure set forth in Sec.s 2.3.1–2.3.3 we may derive recurrence relations that will prove to be identical to the OS relations. Let us examine incrementing the $(ss|ss)$ integral by one angular momentum level. Omitting

---

[2] Strictly, the incomplete Bell polynomials, as all third and higher order derivatives are zero.

normalization, from Eq. 2.18 we have:

$$
\begin{aligned}
(p_i s|ss) &= \frac{1}{2\alpha}\frac{\partial}{\partial A_i}(ss|ss) \\
&= \frac{1}{2\alpha}\frac{\partial}{\partial A_i}K(u)F_0(T) \\
&= \frac{1}{2\alpha}\left(F_0(T)\frac{\partial}{\partial A_i}K(u) + K(u)\frac{\partial T}{\partial A_i}\frac{d}{dT}F_0(T)\right) \\
&= \frac{1}{2\alpha}\left(u_{A_i}K(u)F_0(T) + T_{A_i}K(u)\frac{d}{dT}F_0(T)\right) \\
&= \frac{1}{2\alpha}\left(u_{A_i}(ss|ss) + T_{A_i}\frac{d}{dT}(ss|ss)\right).
\end{aligned}
\tag{2.38}
$$

Let us define the operator $\hat{F}$ as

$$\hat{F} = \frac{d}{dT}. \tag{2.39}$$

$\hat{F}$ operates exclusively on the Boys function, and–as laid out in Eq. 2.12–it functions to transform $F_n(T)$ into $-F_{n+1}(T)$. The last line of Eq. 2.38 can then be written as

$$(p_i s|ss) = \frac{u_{A_i}}{2\alpha}(ss|ss) + \frac{T_{A_i}}{2\alpha}\hat{F}(ss|ss). \tag{2.40}$$

We note that in our notation the Gaussian integral $\hat{F}^m(ij|kl)$ is identical to the auxiliary integral $(ij|kl)^{(m)}$ presented in the OS method and the $(ij|kl)'$ notation in Schlegel [53]. However, the operator notation of Eq. 2.39 is more conducive the discussion set forth in this chapter.

Continuing in this line, we may obtain expressions such as

$$\begin{aligned}
&(p_i p_j|ss) = \frac{1}{4\alpha\beta}\frac{\partial^2}{\partial A_i \partial B_j}(ss|ss) \\
&= \frac{1}{4\alpha\beta}\left((\delta_{i,j}u_{A_i,B_j} + u_{A_i}u_{B_j}) + (T_{A_i}u_{B_j} + u_{A_i}T_{B_j} + \delta_{i,j}T_{A_i,B_j})\hat{F} + T_{A_i}T_{B_j}\hat{F}^2\right)(ss|ss) \\
&= \frac{1}{2\beta}\left(u_{B_j}(\frac{1}{2\alpha}(u_{A_i} + T_{A_i}))(ss|ss) + \frac{\delta_{i,j}}{2\alpha}u_{A_i,B_j}(ss|ss)\right. \\
&\left. + T_{B_j}\hat{F}(\frac{1}{2\alpha}(u_{A_i} + T_{A_i}\hat{F}))(ss|ss) + \frac{\delta_{i,j}}{2\alpha}T_{A_i,B_j}\hat{F}(ss|ss)\right) \\
&= \frac{1}{2\beta}\left(u_{B_j}(p_i s|ss) + \frac{\delta_{i,j}}{2\alpha}u_{A_i,B_j}(ss|ss) + \hat{F}[T_{B_j}(p_i s|ss) + \frac{\delta_{i,j}}{2\alpha}T_{A_i,B_j}(ss|ss)]\right)
\end{aligned} \tag{2.41}$$

We may continue in this fashion to build the entire desired expression.

Alternatively, we may invoke Eq. 2.26. Consider the unnormalized HG ERI, letting $X_{i,x}$ denote the x-th derivative with respect to X_i. The j and k values are held constant and omitted for clarity, but are manipulated in an identical manner.

$$\begin{aligned}
&\frac{1}{2\delta}\frac{\partial}{\partial D_i}(\mathbf{A}_{i,a}\mathbf{B}_{i,b}|\mathbf{C}_{i,c}\mathbf{D}_{i,d}) \\
&= \frac{1}{(2\alpha)^a(2\beta)^b(2\gamma)^c(2\delta)^{d+1}}\frac{\partial^{a+b+c}}{\partial A_i^a \partial B_i^b \partial C_i^c}\frac{\partial^d}{\partial D_i^d}\frac{\partial}{\partial D_i}(\mathbf{A}_{i,0}\mathbf{B}_{i,0}|\mathbf{C}_{i,0}\mathbf{D}_{i,0}) \\
&= \frac{1}{(2\alpha)^a(2\beta)^b(2\gamma)^c(2\delta)^{d+1}}\frac{\partial^{a+b+c}}{\partial A_i^a \partial B_i^b \partial C_i^c}\frac{\partial^d}{\partial D_i^d}\frac{\partial K(u)F_0(T)}{\partial D_i} \\
&= \frac{1}{(2\alpha)^a(2\beta)^b(2\gamma)^c(2\delta)^{d+1}}\frac{\partial^{a+b+c}}{\partial A_i^a \partial B_i^b \partial C_i^c}\frac{\partial^d}{\partial D_i^d}\Big(u_{D_i}K(u)F_0(T) + \hat{F}[T_{D_i}K(u)F_0(T)]\Big) \\
&= \frac{1}{(2\alpha)^a(2\beta)^b(2\gamma)^c(2\delta)^{d+1}}\frac{\partial^{a+b+c}}{\partial A_i^a \partial B_i^b \partial C_i^c}\frac{\partial^d}{\partial D_i^d}\Big(u_{D_i}(\mathbf{A}_{i,0}\mathbf{B}_{i,0}|\mathbf{C}_{i,0}\mathbf{D}_{i,0}) \\
&+ \hat{F}[T_{D_i}(\mathbf{A}_{i,0}\mathbf{B}_{i,0}|\mathbf{C}_{i,0}\mathbf{D}_{i,0})]\Big) \\
&= \frac{1}{(2\alpha)^a(2\beta)^b(2\gamma)^c 2\delta}\frac{\partial^{a+b+c}}{\partial A_i^a \partial B_i^b \partial C_i^c}\Big(\frac{d}{2\delta}u_{D_i,D_i}(\mathbf{A}_{i,0}\mathbf{B}_{i,0}|\mathbf{C}_{i,0}\mathbf{D}_{i,d-1}) \\
&+ u_{D_i}(\mathbf{A}_{i,0}\mathbf{B}_{i,0}|\mathbf{C}_{i,0}\mathbf{D}_{i,d}) + \hat{F}[\frac{d}{2\delta}T_{D_i,D_i}(\mathbf{A}_{i,0}\mathbf{B}_{i,0}|\mathbf{C}_{i,0}\mathbf{D}_{i,d-1}) \\
&+ T_{D_i}(\mathbf{A}_{i,0}\mathbf{B}_{i,0}|\mathbf{C}_{i,0}\mathbf{D}_{i,d})]\Big),
\end{aligned} \tag{2.42}$$

where we have made use of Lemma 1.

Applying the $\frac{\partial^c}{\partial C_i^c}$ derivative, and noting that second derivatives are not functions of the coordinates, we obtain

$$\begin{aligned}
&\frac{1}{(2\alpha)^a(2\beta)^b(2\gamma)^c 2\delta}\frac{\partial^{a+b}}{\partial A_i^a \partial B_i^b}\frac{\partial^c}{\partial C^c}\Big(\frac{d}{2\delta}u_{D_i,D_i}(\mathbf{A}_{i,0}\mathbf{B}_{i,0}|\mathbf{C}_{i,0}\mathbf{D}_{i,d-1}) + u_{D_i}(\mathbf{A}_{i,0}\mathbf{B}_{i,0}|\mathbf{C}_{i,0}\mathbf{D}_{i,d}) \\
&+ \hat{F}[\frac{d}{2\delta}T_{D_i,D_i}(\mathbf{A}_{i,0}\mathbf{B}_{i,0}|\mathbf{C}_{i,0}\mathbf{D}_{i,d-1}) + T_{D_i}(\mathbf{A}_{i,0}\mathbf{B}_{i,0}|\mathbf{C}_{i,0}\mathbf{D}_{i,d})]\Big) \\
&= \frac{1}{(2\alpha)^a(2\beta)^b 2\delta}\frac{\partial^{a+b}}{\partial A_i^a \partial B_i^b}\Big(\frac{d}{2\delta}u_{D_i,D_i}(\mathbf{A}_{i,0}\mathbf{B}_{i,0}|\mathbf{C}_{i,c}\mathbf{D}_{i,d-1}) + \frac{c}{2\gamma}u_{C_i,D_i}(\mathbf{A}_{i,0}\mathbf{B}_{i,0}|\mathbf{C}_{i,c-1}\mathbf{D}_{i,d}) \\
&+ u_{D_i}(\mathbf{A}_{i,0}\mathbf{B}_{i,0}|\mathbf{C}_{i,c}\mathbf{D}_{i,d}) + \hat{F}[\frac{d}{2\delta}T_{D_i,D_i}(\mathbf{A}_{i,0}\mathbf{B}_{i,0}|\mathbf{C}_{i,c}\mathbf{D}_{i,d-1}) \\
&+ \frac{c}{2\gamma}T_{C_i,D_i}(\mathbf{A}_{i,0}\mathbf{B}_{i,0}|\mathbf{C}_{i,c-1}\mathbf{D}_{i,d}) + T_{D_i}(\mathbf{A}_{i,0}\mathbf{B}_{i,0}|\mathbf{C}_{i,c}\mathbf{D}_{i,d})]\Big).
\end{aligned} \tag{2.43}$$

Finally applying the derivatives $\frac{\partial^b}{\partial B_i^b}$ and $\frac{\partial^a}{\partial A_i^a}$, and noting that u_{C_i} and u_{D_i} are constant with respect to them, we obtain

$$\begin{aligned}
&\frac{1}{(2\alpha)^a(2\beta)^b 2\delta}\frac{\partial^{a+b}}{\partial A_i^a \partial B_i^b}\Big(\frac{d}{2\delta}u_{D_i,D_i}(\mathbf{A}_{i,0}\mathbf{B}_{i,0}|\mathbf{C}_{i,c}\mathbf{D}_{i,d-1})\\
&+\frac{c}{2\gamma}u_{C_i,D_i}(\mathbf{A}_{i,0}\mathbf{B}_{i,0}|\mathbf{C}_{i,c-1}\mathbf{D}_{i,d})+u_{D_i}(\mathbf{A}_{i,0}\mathbf{B}_{i,0}|\mathbf{C}_{i,c}\mathbf{D}_{i,d})\\
&+\hat{F}[\frac{d}{2\delta}T_{D_i,D_i}(\mathbf{A}_{i,0}\mathbf{B}_{i,0}|\mathbf{C}_{i,c}\mathbf{D}_{i,d-1})+\frac{c}{2\gamma}T_{C_i,D_i}(\mathbf{A}_{i,0}\mathbf{B}_{i,0}|\mathbf{C}_{i,c-1}\mathbf{D}_{i,d})\\
&+T_{D_i}(\mathbf{A}_{i,0}\mathbf{B}_{i,0}|\mathbf{C}_{i,c}\mathbf{D}_{i,d})]\Big)\\
&=\frac{1}{2\delta}\Big(\frac{d}{2\delta}u_{D_i,D_i}(\mathbf{A}_{i,a}\mathbf{B}_{i,b}|\mathbf{C}_{i,c}\mathbf{D}_{i,d-1})+\frac{c}{2\gamma}u_{C_i,D_i}(\mathbf{A}_{i,a}\mathbf{B}_{i,b}|\mathbf{C}_{i,c-1}\mathbf{D}_{i,d})\\
&+u_{D_i}(\mathbf{A}_{i,a}\mathbf{B}_{i,b}|\mathbf{C}_{i,c}\mathbf{D}_{i,d})+\hat{F}[\frac{d}{2\delta}T_{D_i,D_i}(\mathbf{A}_{i,a}\mathbf{B}_{i,b}|\mathbf{C}_{i,c}\mathbf{D}_{i,d-1})\\
&+\frac{c}{2\gamma}T_{C_i,D_i}(\mathbf{A}_{i,a}\mathbf{B}_{i,b}|\mathbf{C}_{i,c-1}\mathbf{D}_{i,d})+\frac{b}{2\beta}T_{B_i,D_i}(\mathbf{A}_{i,a}\mathbf{B}_{i,b-1}|\mathbf{C}_{i,c}\mathbf{D}_{i,d})\\
&+\frac{a}{2\alpha}T_{A_i,D_i}(\mathbf{A}_{i,a-1}\mathbf{B}_{i,b}|\mathbf{C}_{i,c}\mathbf{D}_{i,d})+T_{D_i}(\mathbf{A}_{i,a}\mathbf{B}_{i,b}|\mathbf{C}_{i,c}\mathbf{D}_{i,d})]\Big).
\end{aligned} \tag{2.44}$$

Eq. 2.44 is Schlegel's derivative theorem. It is true for any HG ERI, and for CG ERIs composed solely of s- and p-type orbitals.

To relate Eq. 2.44 to the the OS method, and hence solve d-type and higher CG ERIs, we re-express the CG ERI as a linear combination of HG ERIs through use of Eq. 2.19 [3]. Combining the formulae of Eq. 2.19 and Eq. 2.44, and letting $(\mathbf{A}_{i,a}\mathbf{B}_{i,b}|\mathbf{C}_{i,c}\mathbf{D}_{i,d})^C$ represent the linear combination of HGs that creates the CG with angular momentum a in the i-

---

3. Note that endnote (10) of Ref. [26] refers to, but does not describe, this method of deriving the OS-VRR.

coordinate for center **A** etc., we obtain the OS relation

$$
\begin{aligned}
&(\mathbf{A}_{i,a}\mathbf{B}_{i,b}|\mathbf{C}_{i,c}\mathbf{D}_{i,d+1})^{C} = \\
&\frac{1}{2\delta}\Big(d\ (\frac{1}{2\delta}u_{D_i,D_i}+1)(\mathbf{A}_{i,a}\mathbf{B}_{i,b}|\mathbf{C}_{i,c}\mathbf{D}_{i,d-1})^{C}+\frac{c}{2\gamma}u_{C_i,D_i}(\mathbf{A}_{i,a}\mathbf{B}_{i,b}|\mathbf{C}_{i,c-1}\mathbf{D}_{i,d})^{C} \\
&+u_{D_i}(\mathbf{A}_{i,a}\mathbf{B}_{i,b}|\mathbf{C}_{i,c}\mathbf{D}_{i,d})^{C}+\hat{F}[\frac{d}{2\delta}T_{D_i,D_i}(\mathbf{A}_{i,a}\mathbf{B}_{i,b}|\mathbf{C}_{i,1}\mathbf{D}_{i,d-1})^{C} \\
&+\frac{c}{2\gamma}T_{C_i,D_i}(\mathbf{A}_{i,a}\mathbf{B}_{i,b}|\mathbf{C}_{i,c-1}\mathbf{D}_{i,d})^{C}+\frac{b}{2\beta}T_{B_i,D_i}(\mathbf{A}_{i,a}\mathbf{B}_{i,b-1}|\mathbf{C}_{i,c}\mathbf{D}_{i,d})^{C} \\
&+\frac{a}{2\alpha}T_{A_i,D_i}(\mathbf{A}_{i,a-1}\mathbf{B}_{i,b}|\mathbf{C}_{i,c}\mathbf{D}_{i,d})^{C}+T_{D_i}(\mathbf{A}_{i,a}\mathbf{B}_{i,b}|\mathbf{C}_{i,c}\mathbf{D}_{i,d})^{C}]\Big).
\end{aligned}
\tag{2.45}
$$

For consistency with earlier works, we refer to the eight-term recursion relation in Eq. 2.45 simply as the vertical recurrence relation (VRR).

2.3.5 Discussion and Conclusions

The OS-VRR–and the refinements and expansions of Pople, Head-Gordon, and others [26, 21, 20]–are among the most powerful methods available for rapid electronic-structure calculations. Unfortunately, the derivations given in standard texts tend to only derive the OS-VRR in an indirect fashion via overlap and other integrals. Furthermore, the relation between the OS method and Schlegel's derivative theorem is almost always overlooked, despite its fundamental significance in elucidating the nature of the OS-VRR. It is hoped that this work will help to rectify the shortcoming, and alleviate some of the difficulties experienced in approaching the study of Gaussian integral evaluation.

CHAPTER 3

EFFECTS OF NITROGEN SUBSTITUENT GROUPS ON THE BENZENE DICATION

3.1 Benzene Dications

3.1.1 Background

There has been much interest in the benzene dication [32, 17], and recent works have experimentally verified the lowest energy structure of the benzene dication [29] and the closely related hexamethylbenzene dication [37] as a pentagonal-pyramidal structure (nido cluster), as predicted by analogy to the Wade rules for boranes.

In a similar vein, a number of papers have been published regarding the structures of various halogenated benzene dications and related dications [50, 11, 25, 31], and their differences from the parent benzene dication. In contrast, relatively little research has been done on nitrogen containing dications of benzene derivatives [3] and the effects of nitrogenous substituents on the structure of the dication.

Benzene dications and their derivatives are of interest due to both their ability to form hypercoordinated carbons and their unusually long carbon-carbon bonds. These points are of particular significance in light of recent discoveries of the role of hexacoordinated carbon in catalyzing the reduction of N_2 to ammonia in biological systems [33].

3.1.2 Methods

In this letter we present electronic-structure findings regarding the lowest energy structure of the aniline and nitrobenzene dications. To differentiate the effects of the nitrogenous substituent from simple steric effects, we contrast our findings with structures of the toluene dication.

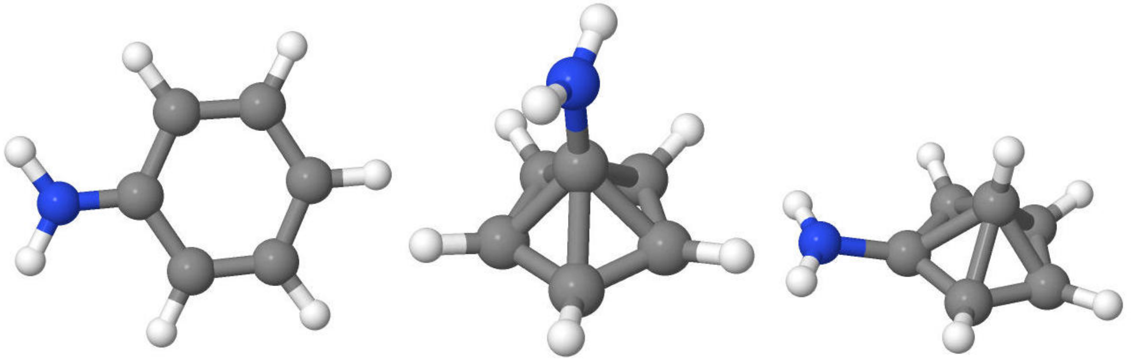

(a) Flat (b) Apical Pentagonal-Pyramidal (c) Ring Pentagonal-Pyramidal

Figure 3.1: Dication Geometries

The geometries of the cations of toluene, aniline, and nitrobenzene were optimized using MP2 with the cc-pVTZ basis set. Single point calculations were run on the optimized geometries using coupled-cluster with single and double excitations and non-iterative triples corections (CCSD(T)) using the cc-pVDZ basis set and, when possible, the cc-pVTZ basis set as well. These findings are contrast with calculations run using parametric reduced-density-matrices (p2-RDM), also in the cc-pVTZ basis set.

In particular, the three geometries in Fig. 3.1 were closely examined: (1) A flat hexagon, similar to the parent benzene molecule, (2) a pentagonal-pyramidal structure with the substituent attached to the apical carbon, and (3) a pentagonal-pyramidal structure with the substituent attached to a carbon on the ring. Other geometries related to different conformers of hexane, such as a chair conformation, where also explored. It was found that after geometry optimization these conformers converged to Fig. 3.1(a).

3.1.3 Results

As shown in Table 3.1, the toluene dication exhibited notably greater stability in a pentagonal-pyramidal structure than in a flat structure–which was prone to expelling a proton. The difference in energy between the two possible pentagonal-pyramidal structures was quite

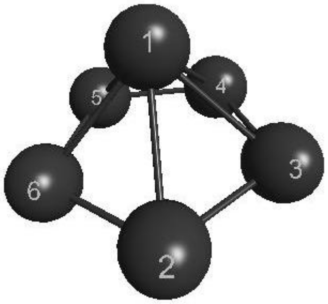

Figure 3.2: Numbering scheme for pentagonal-pyramidal carbon skeleton. Note that for the ring pentagonal-pyramidal isomer, the carbon bonded to the substituent is always labeled as 2.

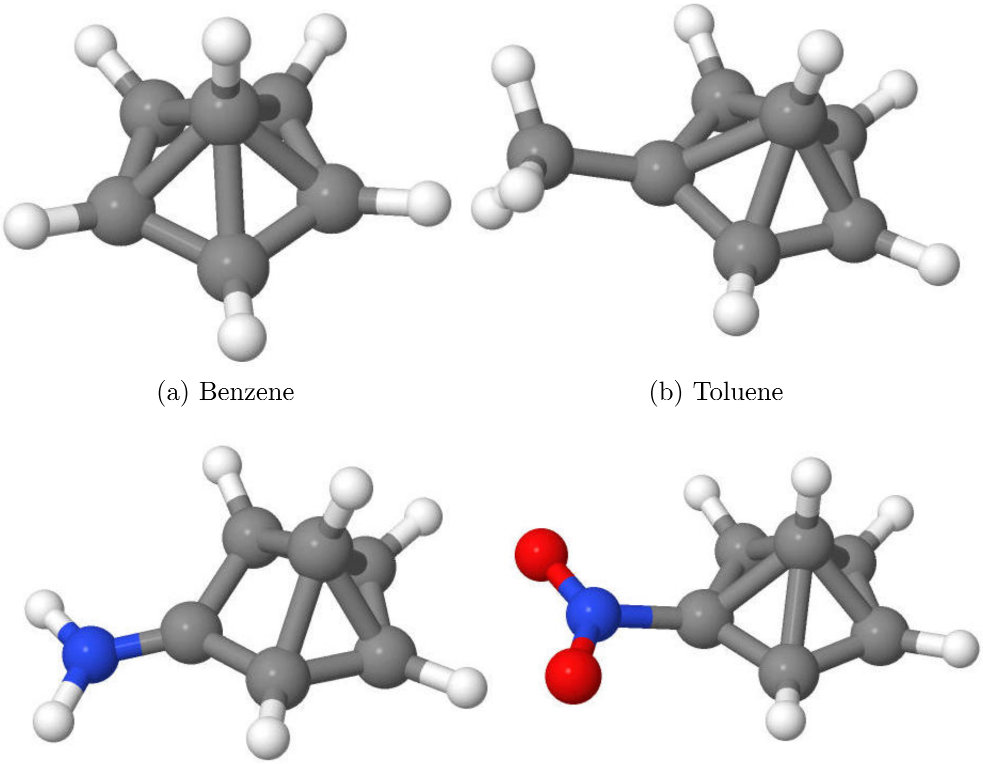

(a) Benzene

(b) Toluene

(c) Aniline

(d) Nitrobenzene

Figure 3.3: Geometry Optimized Pentagonal-Pyramidal Dications

Table 3.1: Coupled-Cluster Energies and Relative Stabilities of Substituted Benzene Dications Isomers. The second column gives the energy for the pentagonal-pyramidal isomer with the substituent apical. The third and fourth columns give the relative stability of the ring pentagonal-pyramidal structure over the apical pentagonal-pyramidal and flat isomers. Energy is in Hartrees (results from CCSD(T) in the cc-pVTZ basis set unless otherwise noted).

Dication	Ring Pentagonal-Pyramidal	ΔE to Apical Pentagonal-Pyramidal	ΔE to Flat
Benzene	-230.932	+0.000	+0.024
Hexamethylbenzene[1]	-466.301	+0.000	+0.049
Toluene	-270.201	-0.001	+0.006
Aniline	-286.280	+0.049	-0.028
Nitrobenznene[2]	-434.704	+0.104	+0.033

1. Results from Ref. [37] in MP2 in the cc-pVTZ basis set for near flat chair isomer.
2. Calculations done with CCSD(T) in the cc-pVDZ basis set.

Table 3.2: p2-RDM Energies and Relative Stabilities of Substituted Benzene Dications Isomers. The second column gives the energy for the pentagonal-pyramidal isomer with the substituent apical. The third and fourth columns give the relative stability of the ring pentagonal-pyramidal structure over the apical pentagonal-pyramidal and flat isomers. Energy is in Hartrees (results from p2-RDM in the cc-pVTZ basis set unless otherwise noted).

Dication	Ring Pentagonal-Pyramidal	ΔE to Apical Pentagonal-Pyramidal	ΔE to Flat
Benzene	-230.915	+0.000	+0.022
Hexamethylbenzene[3]	-466.301	+0.000	+0.049
Toluene	-270.184	$+5.77 \times 10^{-4}$	+0.003
Aniline	-286.262	+0.051	-0.030
Nitrobenznene	-435.084	+0.098	+0.025

3. Results from Ref. [37] in MP2 in the cc-pVTZ basis set for near flat chair isomer.

small, with the identification of the favored structure differing between Fig. 3.1(b) according to the CCSD(T) calculations (Table 3.1), and Fig. 3.1(c) according to the p2-RDM calculations (Table 3.2). The ring pentagonal-pyramidal structure demonstrated moderate steric effects in that the four ring carbons not attached to the methyl group (carbons $3 - 6$, or C3−C6, in Fig. 3.2) had a bond length of 1.658 Å to the apical carbon (C1), while the ring carbon attached to the methyl group (C2) was 1.747 Å from the apical carbon, indicating a lower degree of bonding.

As shown in Fig. 3.3(c), in the ring pentagonal-pyramidal configuration, the aniline dication exhibits far greater distortion from an ideal pentagonal-pyramid than the other molecular ions, with the ring carbon attached to the amino group (C2) over two angstroms from the apical carbon (C1), indicating a near zero bond-order between the carbons. Related to aniline's inability to form an ideal pentagonal-pyramid, calculations (Tables 3.1 & 3.2) indicate that the most stable geometry is the flat hexagon of Fig. 3.1(a). It should be noted

Table 3.3: Bond Length Between Apical and Ring Carbon. Length in Angstroms (results from structure optimized with MP2 in the cc-pVTZ basis set unless otherwise noted).

Dication	Apical (where Applicable)	Ring
Benzene	1.672 Å	
Hexamethylbenzene[4]	1.705 ± 0.011 Å	
Toluene	1.696 ± 0.002 Å	1.703 ± 0.045 Å
Aniline	1.616 ± 0.044 Å	1.625 ± 0.020 Å[5]
Nitrobenznene	1.682 ± 0.011 Å	1.679 ± 0.015 Å

1. Experimental results from Ref. [37].

that the carbon skeleton of the aniline dication possesses D_{2h} symmetry due to compression of the molecule along the axis of the $C - N$ bond.

In strong contrast to aniline, the nitrobenzene dication is most stable in the ring pentagonal-pyramidal structure of Fig. 3.1(d). In this geometry the nitrobenzene dication shows minimal distortion from the benzene dication. The carbon skeleton is close to C_{5v} symmetry, with the bonds between the ring and the apical carbon varying from 1.694 Å for the bond between the apical carbon and the carbon bonded to the nitro group (C1 to C2) to 1.664 Å for the bond between the apical carbon and the ring carbons opposite the nitro group (C1 to C4 & C5).

3.1.4 Discussion and Conclusions

Aniline's greater stability in a flat geometry and inability to form an ideal pentagonal-pyramid stand to reason. The nitro group is a strongly electron withdrawing, while the amino group is strongly electron donating. Thus the amino group favors greater electron-density in the carbon skeleton, more closely resembling aromatic electronic structure of the parent aniline molecule. Inversely, the nitro group depletes electron density from the carbon skeleton, further skewing the structure towards a nido cluster. This is supported by both Mulliken and Löwdin population analyses, which demonstrate around $0.3 - 0.4$ higher electron population in the carbon skeleton of aniline than that of nitrobenzene. Accordingly, the relative stability between the ring pentagonal-pyramidal nitrobenzene to its flat isomer is larger than the relative stability between the pentagonal-pyramidal and flat benzene dication (Tables 3.1 & 3.2).

For both the aniline and nitrobenzene dications, the apical pentagonal-pyramidal structure of Fig. 3.1(b) was notably less stable the the ring pentagonal-pyramidal structure of Fig. 3.1(c). For the toluene dication the two structures are essentially identical in energy, indicating the difference does not stem from steric effects. Instead, the difference appears to originate in nitrogen's affinity for a double bond to stabilize its charge. When the nitrogenous substituent is placed in the apical position, the apical carbon (C1)–which possesses partial bonds to the five ring carbons (carbons $2-6$)–has a $C-N$ bond order of 0.98 (nitrobenzene) or 1.5 (aniline). In contrast, when the substituent is placed on the ring position, the $C-N$ bond order increases to 1.5 (nitrobenzene) or 1.7 (aniline). In terms of basic organic chemistry, this can be understood as ring pentagonal-pyramidal isomer having more favorable resonance structures than the apical pentagonal-pyramidal structure.

In conclusion, we have calculated the most stable structure of the aniline and nitrobenzene dications. Placing a substituent on a ring carbon of a pentagonal-pyramidal structure results in moderate steric distortion of the structure, as seen in Table 3.3. The steric effect is far too small to explain the large distortion displayed by the ring pentagonal-pyramidal aniline dication. Instead, we demonstrate that the aniline dication has too high an electron-density in its skeleton to follow the Wade rules, and instead retains a compressed hexagonal geometry. Nitrobenzene, owing to the depletion of electron-density in the skeleton, forms a near ideal pentagonal-pyramid in accordance with the Wade rules, exhibiting a greater relative stability than either the toluene or benzene dications. For either nitrogenous substituent, there is a strong preference to place the substituent on the ring rather than the apical position.

We note that p2-RDM compares highly favorably to CCSD(T). This is of particular interest as the hexacoordinated apical carbon in the pentagonal-pyramidal geometry differs substantially from standard organic molecules. For the cases of benzene, toluene, and aniline (for which the same basis sets where used), the absolute energies did not differ by more than

0.018 Hartrees (11 kCal/mol). More significantly, the energy differences between isomers agreed to a maximum difference of 0.003 Hartree (2 kCal/mol), indicating that p2-RDM is a viable method for calculating the lowest energy isomer of substituted benzene dications, despite its lower computational cost.

CHAPTER 4

RELATIONS BETWEEN ENVIRONMENTAL NOISE AND ELECTRONIC COUPLING FOR OPTIMAL EXCITON TRANSFER IN ONE- AND TWO-DIMENSIONAL HOMOGENEOUS AND INHOMOGENEOUS QUANTUM SYSTEMS

This chapter contains parts of a published work [C. C. Forgy and D. A. Mazziotti J. Chem. Phys. 141, 224111 (2014)] Copyright 2014, American Institute of Physics.

4.1 Introduction

Many recent studies have focused on the possibility of using environmental noise to enhance the efficiency of excitonic transport [48, 30, 43, 47, 19, 41, 55, 64, 28]. This research was originally motivated in large part by studies indicating surprisingly long-lived quantum coherence in biological systems [18, 14], which prompted study into the interplay of quantum coherence and environmental noise. Light excites a molecular moiety of a quantum system. The energy of the light in the form of the excitation (or *exciton*) then moves through the system until it reaches a sink which extracts the energy. In addition to the significance of excitonic transfer in inhomogeneous biological systems, excitonic transfer also plays a role in homogeneous systems such as quantum-dot devices [12, 10, 59], charge transfer in carbon nanotubes [23] and organic photovoltaics [35, 51]. Research has in particular focused on dephasing noise, which is believed to well approximate general broad environmental noise [43, 47].

Previous research has found that maximal transport efficiency will be obtained at a *finite* dephasing rate when dephasing noise is beneficial to the system and has quantified the optimal dephasing rate as a function of both dissipation and sink coupling strength [30]. The current work extends previous studies [30, 47, 42, 8, 9] by examining the relationship between the coupling strength between chromophores and the optimal dephasing rate. We demonstrate that not only does an optimal dephasing rate exist in both one- and two-dimensional networks but also that it increases in magnitude with increasing coupling strength between chromophores. We further demonstrate that this relation will only obtain in homogeneous or near homogeneous systems. In inhomogeneous systems the optimal dephasing rate will be largely determined by the network connectivity, and will only be slightly affected by changes in coupling strength. We also examine the relationship between transport efficiency and the computed entanglement of the chromophores and show that optimal transport occurs when the noise quenches the entanglement between local modes that prevent the exciton from moving efficiently to the target site. These trends in optimal dephasing with coupling strength in the context of homogeneous and inhomogeneous systems provide guidelines that have potential applicability to optimizing energy-transfer efficiency in materials such as quantum dot arrays [10] and carbon nanotubes [23] that resemble the one- and two-dimensional systems discussed in this chapter.

4.2 Theory

After presenting the theoretical model of the Hamiltonian for both one- and two-dimensional homogeneous quantum systems in Section 4.2.1, we discuss the time-evolution density-matrix equations in the presence of environmental noise in Section 4.2.2. In Section 4.2.3 we discuss modifications of the Hamiltonian for inhomogeneous systems. In Section 4.2.4 we discuss the effect of sink coupling and environmental dissipation.

4.2.1 Homogeneous Model

The Hamiltonian for our system is

$$\hat{H} = \sum_{i,j} A e^{-\alpha \|i-j\|_2} |i\rangle\langle j| \tag{4.1}$$

where $A = 100$ a.u. unless otherwise specified, $|i\rangle$ denotes the i^{th} chromophore (site), and α is an adjustable parameter with arbitrary units of reciprocal length. The α parameter in Eq. (4.1) can approximately model a power law dependence in situations such as dipole-dipole interactions. The 2-norm $\| i - j \|_2$ measures the Euclidean distance between the lattice points i and j. In both chains and two-dimensional lattices the distance between adjacent sites i and j is defined to be 1 (arbitrary units); consequently, in the two-dimensional lattices the distance between i and j separated across the diagonal of the square is $\sqrt{2}$. Note that the sites are homogeneous and are described by the energy A.

This Hamiltonian is used to describe the coupling of two different networks: (1) A linear chain nine sites long, where the exciton is localized at site 1 at the initial time, and the trapping site is attached either to site 5 (end-to-middle transport) or site 9 (end-to-end transport), and (2) A five-by-five two-dimensional grid of sites where the exciton begins in site 1, and the trapping site is attached to the central site, site 13. Since changing the value of A will change the kinetics of the system but not the overall trends discussed in this chapter, a value of $A = 100$ a.u. is used throughout this chapter. In a real system A can be rescaled to reflect the phenomenological data or predicted site energies of the material.

The strength of coupling to the sink and the dissipation rate where chosen to be those previously used for the Fenna-Matthews-Olson (FMO) complex even for the homogeneous systems [39, 56, 1]. This will allow for easier comparisons to the results of inhomogeneous systems in Section 4.3.5. In atomic units (wavenumbers) the rates are 1.21×10^{-8} (0.00266 cm^{-1}) for the sink coupling and 7.26×10^{-5} (15.9 cm^{-1}) for the dissipation rate. By using low-to-moderate values for both dissipation and sink coupling, we ensure that dephasing-assisted transport is possible [30], a point that will be elaborated upon in section 4.2.4.

4.2.2 Quantum Liouville Equation

As described in Sec. 1.2.2, the density matrix of an open quantum system evolves in time according to the quantum Liouville equation with the Lindblad operator

$$\frac{d}{dt}D = -\frac{i}{\hbar}[\hat{H}, D] + \hat{L}(D) \tag{4.2}$$

where D is the density matrix [1]. The addition of the Lindblad operator provides a general treatment for the time dynamics of open quantum systems in the Markovian approximation [34]. The Lindblad operator $\hat{L}(D)$ can be divided into three operators which create the dephasing, dissipation, and capture of the exciton by the sink

$$\hat{L}(D) = \hat{L}_{\text{deph}}(D) + \hat{L}_{\text{diss}}(D) + \hat{L}_{\text{sink}}(D) \tag{4.3}$$

in which

$$\begin{aligned}
\hat{L}_{\text{deph}}(D) &= a\sum_{e} 2\langle e|D|e\rangle|e\rangle\langle e| - \{|e\rangle\langle e|, D\}, && (4.4)\\
\hat{L}_{\text{diss}}(D) &= b\sum_{e} 2\langle e|D|e\rangle|g\rangle\langle g| - \{|e\rangle\langle e|, D\}, && (4.5)\\
\hat{L}_{\text{sink}}(D) &= 2c\langle \kappa|D|\kappa\rangle|s\rangle\langle s| - c\{|\kappa\rangle\langle \kappa|, D\}, && (4.6)
\end{aligned}$$

where $|g\rangle$ and $|e\rangle$ denote the ground and excited states of the Hamiltonian, respectively, $|s\rangle$ is the sink, and $|\kappa\rangle$ is the site chosen to couple to the sink. The ordinary differential equations were solved using the fourth-fifth order Runge-Kutta-Fehlberg method implemented in the computer algebra system Maple [2].

In these definitions we assume that the sink is distinct from the sites on the chain. Some previous papers have instead selected the sink site be one of the sites on the chain [30]. We

---

[1] Note the use of D instead of ρ.

[2] Maple 16. Maplesoft, a division of Waterloo Maple Inc., Waterloo, Ontario. Maple is a trademark of Waterloo Maple Inc.

found that the overall trends were unchanged when we modified Eq. (4.6) to place the sink in the chain. As stated in section 4.2.1, in atomic units $b = 7.26 \times 10^{-5}$ and $c = 1.21 \times 10^{-8}$. Throughout the chapter the dissipation rate a is reported in units of the rate used for the FMO complex with an a of 1 corresponding to 1.52×10^{-4} a.u. (33.4 cm^{-1}).

4.2.3 Hamiltonian for Inhomogeneous Systems

For inhomogeneous systems we replace the Hamiltonian in Eq. (4.1) with the Hamiltonian of the FMO complex in Ref. [47], originally produced in Ref. [1]. The Hamiltonian $\hat{H}$ is given by the matrix

$$\begin{pmatrix} 215.0 & -104.1 & 5.1 & -4.3 & 4.7 & -15.1 & -7.8 \\ -104.1 & 220.0 & 32.6 & 7.1 & 5.4 & 8.3 & 0.8 \\ 5.1 & 32.6 & 0.0 & -46.8 & 1.0 & -8.1 & 5.1 \\ -4.3 & 7.1 & -46.8 & 125.0 & -70.7 & -14.7 & -61.5 \\ 4.7 & 5.4 & 1.0 & -70.7 & 450.0 & 89.7 & -2.5 \\ -15.1 & 8.3 & -8.1 & -14.7 & 89.7 & 330.0 & 32.7 \\ -7.8 & 0.8 & 5.1 & -61.5 & -2.5 & 32.7 & 280.0 \end{pmatrix}$$

where the elements are given in the unit of 4.5620×10^{-6} a.u., and the zero of energy has been shifted by 1.2230×10^{4}. The coupling strengths of the FMO complex are re-scaled by multiplying the off-diagonal elements of the Hamiltonian by $e^{-\alpha}$, thus $\alpha = 0$ is the baseline FMO complex Hamiltonian. The cases of $\alpha < 0$ correspond to increasing the coupling strength to greater than that defined in the FMO model. In order to further compare the results of the FMO complex to the homogeneous system, we also ran simulations in which the FMO complex was treated as a linear system and the off-diagonal elements decayed as $e^{-\alpha\delta}$ (as in Eq. (4.1), where $\delta = \| i - j \|_2$), and simulations where only nearest neighbor couplings were allowed.

4.2.4 Other Effects

In Ref. [30], it is reported that dephasing-assisted transport is only possible when both coupling to the sink and environmental dissipation are relatively weak. Excessively weak sink coupling will slow the kinetics to the point where the exciton is likely to be lost before capture. Similarly, excessively strong coupling will present too high a potential barrier for the particle to enter the sink. The existence of an optimal sink coupling rate and the detrimental effects of excessively strong sink coupling are also reported by Ref. [19]. As mentioned in Sec.s 4.2.1 & 4.2.2, we use a moderate sink coupling value throughout this chapter.

In the chosen model dissipation is monotonically detrimental to excitonic transport. However, we note that the authors of [8] have demonstrated that in specialized systems dissipation can be beneficial to transport. In the presented model, if the dissipation noise is too strong, the exciton will be lost before entering the sink. However, as the rate of decrease in transport efficiency with respect to increasing dissipation noise is relatively low, our findings should be qualitatively true across a wide range of dissipation levels.

4.3 Results

4.3.1 End-to-End Homogeneous Transport

Results for a linear chain of nine sites with full coupling are presented in Fig. 4.1. It should be noted that the unphysically strong case of $\alpha = 0$, in which the site energies and the coupling strengths are equal to 100 a.u., is isomorphic to the physical case of nine sites in which each one is connected to every other one in a net-like arrangement. For the net-like case of $\alpha = 0$, all sites are equivalent, and thus it is meaningless to refer to 'end-to-end' or 'end-to-middle' transport.

As can be seen from Fig. 4.1, for the case of $\alpha = 0$ dephasing noise strongly facilitates excitonic transport until the dephasing rate a equals 24 (in units of 1.52×10^{-4} a.u.). This is unsurprising because, as mentioned, $\alpha = 0$ is not a true case of end-to-end transport. What

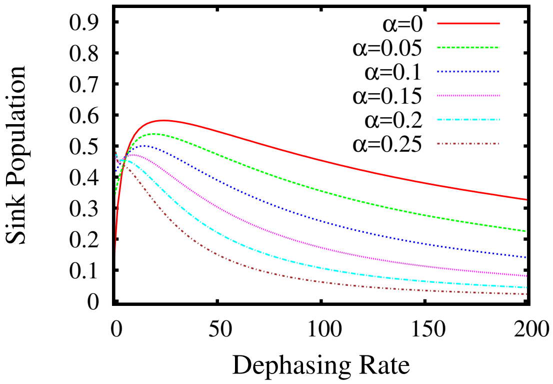

Figure 4.1: The sink population after 1 picosecond for a linear homogeneous chain with the sink attached to the *end site* is reported as a function of the dephasing parameter a for different coupling parameters α. Because α is the decay parameter in Eq. (4.1), the coupling strength decreases with increasing α. For low coupling strengths (i.e. $\alpha \geq 0.25$) the optimal dephasing rate is zero; for higher coupling strengths the optimal dephasing rate is finite. The largest optimal dephasing rate occurs for the largest coupling between chromophores at $\alpha = 0$.

is surprising is that dephasing noise remains beneficial for end-to-end transport–though less strongly so–until α reaches a value of about 0.15.

We posit that this is because in the extremely strong coupling region of $\alpha \lesssim 0.2$ the topology will retain substantial net-like, rather than chain-like characteristics. It is only in the strictly chain-like weaker region of $\alpha \gtrsim 0.2$ that dephasing-assisted transport becomes impossible for end-to-end transport, as reported in previous research [30]. We note that dephasing enhanced transport is only due to the net-like topology, and thus will be impossible in the case of nearest-neighbor coupling, consistent with the prior findings [30].

4.3.2 End-to-Middle Homogeneous Transport

We next turn to the case of end-to-middle transport. We again have a chain nine sites long with full exponential coupling, but now the sink is attached to the middle (fifth) site. This is the case that, according to [30], should show the strongest possible dephasing-assisted transport, at least for nearest neighbor coupling. This is also one of the topologies reported in [19], where it is claimed that it will exhibit a finite optimal dephasing rate.

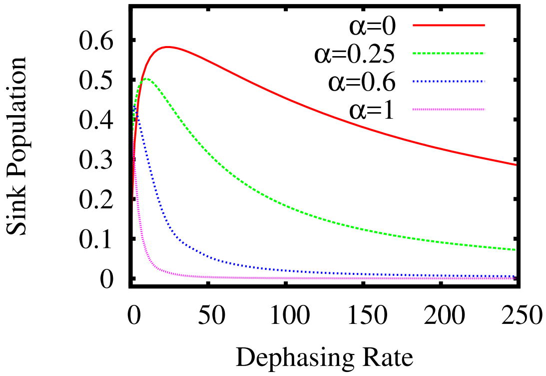

Figure 4.2: The sink population after 1 picosecond for a linear homogeneous chain with the sink attached to the *middle site* is reported as a function of the dephasing parameter a for different coupling parameters α. For low coupling strengths (i.e. $\alpha \geq 1$) the optimal dephasing rate is zero; for higher coupling strengths the optimal dephasing rate is finite. The largest optimal dephasing rate occurs for the largest coupling between chromophores at $\alpha = 0$.

As can be seen in Fig. 4.2, dephasing can facilitate exciton transport for strong coupling. For the unphysically strong coupling of $\alpha = 0$ (i.e. all sites and all coupling energies are 100), the sink population after 1 ps starts at 0.097 without dephasing and rises almost sixfold to a maximum value of 0.58 at the optimal dephasing rate of 24 times the base rate before slowly decreasing again.

The same trend is observed, albeit less dramatically, for the very strong coupling of $\alpha = 0.25$. For the more realistic case of $\alpha = 0.6$, we obtain a maximum sink population of 0.44, 112% of the population of 0.39 obtained without dephasing, at an optimal dephasing rate of about 1.75 times the base dephasing rate. At $\alpha = 1$, it is found that dephasing no longer has any possible benefit, and indeed is strongly detrimental to excitonic transfer.

These finding are summarized in Fig. 4.3, where we define the optimal dephasing rate as the rate that produces the highest exciton trapping after 1 ps (rather than the maximum trapping at infinite time). As can be seen from (a), the optimal dephasing rate is maximal for $\alpha = 0$, and falls essentially exponentially until it reaches a value of about zero around $\alpha = 0.85$, at which point dephasing-assisted transport is no longer possible. Fig. 4.3 (b) shows

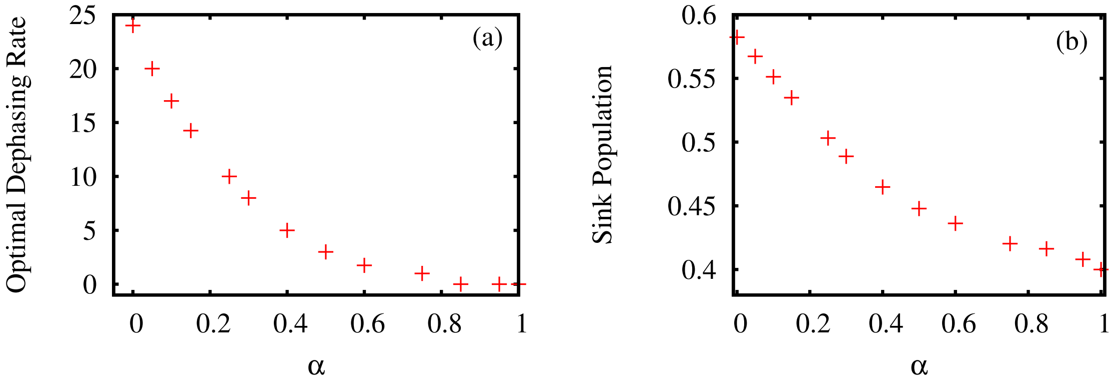

Figure 4.3: For a homogeneous chain of nine sites with the sink attached to the middle site we show (a) the optimal dephasing rate and (b) the sink population after 1 ps (when the optimal dephasing rate from (a) is employed) as functions of the coupling between chromophores α. Both the optimal dephasing rate and the sink population at 1 ps from that rate increase with increasing coupling strength. Note that because α is the decay parameter in Eq. (4.1), the coupling strength decreases with increasing α.

the sink population after 1 picosecond when the system evolves at its optimal dephasing rate. The sink population is highest for the strongest coupling values, and falls monotonically as the coupling strength decreases.

An intuitive understanding of this phenomenon can be given as follows: The effect of strong coupling between sites is to send a substantial portion of the exciton population to the off-diagonal 'superposition' states. This, somewhat paradoxically, results in a manifestation of localization in which the exciton population is trapped in a primarily local-mode bipartite entanglement between two sites at a time (see Fig. 4.8). As dephasing is introduced, it disrupts the local-mode entanglement and allows for non-local or delocalized modes across the system. As can also be seen from Fig. 4.2, in a system with no dephasing, stronger coupling will in fact inhibit exciton transfer. This is due to the fact that, without dephasing noise, the local-mode bipartite entanglement will be the strongest, leaving little opportunity for non-local modes.

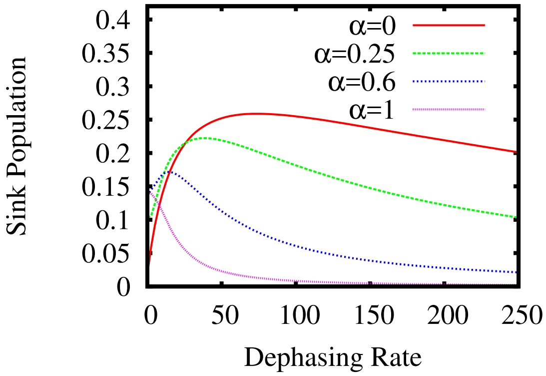

Figure 4.4: The sink population after 1 picosecond for a 5×5 grid with the sink attached to the middle site is reported as a function of the dephasing parameter a for different coupling parameters α. As in the one-dimensional (linear) quantum systems, the optimal dephasing rate increases with increasing coupling strength, and the largest optimal dephasing rate occurs for the largest coupling between chromophores at $\alpha = 0$.

4.3.3 Transport in a Homogeneous Array

Simulations were run for a two-dimensional array with full exponential coupling, where the Hamiltonian is described by Eq. (4.1). This is more physically similar to a case that may be encountered in man-made materials, such as an array of light harvesting quantum dots. The results obtained were remarkably similar to those obtained in the one-dimensional case.

Fig. 4.4 presents the results of a five-by-five grid with the sink attached to the middle (thirteenth) site. As in the case of end-to-middle one-dimensional transport, dephasing-assisted transport is specifically beneficial for cases with stronger coupling, and stronger coupling without dephasing exhibits notably worse transfer kinetics than weak coupling without dephasing. Owing to the larger size of the system–twenty-five sites as opposed to nine–and the ensuing potentially larger path length, the exciton population trapped after 1 ps is uniformly less than the corresponding cases in the chain. As in section 4.3.1, when the sink is attached to the site on the opposite corner from the initial site, dephasing enhanced transport is impossible for all but the strongest of couplings.

Table 4.1: The sink population after 1 ps for a homogeneous chain of nine chromophores with *site defects* in the presence of optimal dephasing. The symbol 100:100 refers to the case in which all sites are equal to 100, and the symbol 101:99 refers to the case of site energies alternating between 101 and 99. Regardless of the coupling strength α between sites, we find that the site defects do not significantly affect the exciton population reaching the sink.

	Sink Population After 1 ps				
α	100 : 100	101 : 99	99 : 101	110 : 90	90 : 110
0	0.582	0.583	0.582	0.584	0.581
0.25	0.503	0.504	0.503	0.510	0.497
0.6	0.436	0.440	0.433	0.472	0.406
1	0.400	0.407	0.392	0.441	0.312

4.3.4 Site Defects

We next introduce inhomogeneity into a chain of nine chromophores. In Table 4.1 we present results for cases where the site energies vary between 101 and 99 (starting with both 101 and 99), and between 110 and 90, along with the above results for a degenerate chain with all site energies equal to 100. In all these cases, the off diagonal coupling energy is still defined as $100e^{-\alpha\|i-j\|_2}$, where 100 is the average energy between adjacent sites.

As can be seen from Table 4.1, there is little variation in sink population after 1 ps for the different cases. When the exciton starts in a site with higher energy than its nearest neighbor (101 or 110), there is a slight bias to force the exciton out of the site which results in a slightly higher sink population. By the same logic, if the exciton starts in a site with lower energy than its nearest neighbor (99 or 90), there is a slight bias against moving the exciton, which results in a lower sink population. We note that this trend is particularly pronounced for higher α values, where coupling is primarily nearest neighbor coupling.

We further note that, as can seem from Table 4.2, when the exciton begins in a lower energy site, the optimal dephasing rate slightly increases, while it generally slightly decreases when the exciton begins in a higher energy site. We posit that this is due to the fact that when the exciton begins in a lower energy site, classical (hopping) transport is further disfavored

Table 4.2: The optimal dephasing rates for the homogeneous 9-site chain with site defects discussed in Table 4.1. When the exciton begins in a lower energy site, the optimal dephasing rate increases slightly, while it generally decreases slightly when the exciton begins in a higher energy site. Importantly, the general trend of the optimal dephasing increasing with increasing coupling strength α remains true in the presence of site defects. A dephasing rate of 1 is defined as the value (1.52×10^{-4} a.u.) found in the FMO complex.

	Optimal Dephasing Rates				
α	100 : 100	101 : 99	99 : 101	110 : 90	90 : 110
0	24	24	24	23.75	24.5
0.25	10	9.75	10	9.5	10.25
0.6	1.75	1.5	1.75	0.85	2.5
1	0	0	0	0.25	1

Table 4.3: The sink population after 1 ps and its optimal dephasing are reported for the FMO complex with its off-diagonal coupling elements multiplied by $e^{-\alpha}$(columns 2 and 3) and the linearized FMO complex with its off-diagonal coupling elements multiplied by $e^{-\alpha\delta}$ (where $\delta = \| i - j \|_2$). The optimal dephasing rate remains *essentially constant* with changes in the coupling strength.

	FMO Hamiltonian with Off-diagonal Elements Altered			
α	Dephasing Rate for $e^{-\alpha}$	Sink Population for $e^{-\alpha}$	Dephasing Rate for $e^{-\alpha\delta}$	Sink Population for $e^{-\alpha\delta}$
-0.6	3.25	0.601		
-0.1	3.40	0.376		
0	3.60	0.326	3.60	0.326
0.1	3.80	0.280	4.25	0.281
0.25	4.05	0.219	4.00	0.218
0.6	4.30	0.115	4.35	0.111
1	4.05	0.050	4.10	0.047

requiring higher dephasing to optimize quantum transport. Similarly, starting the exciton in a higher energy site favors classical transport. The effect of dephasing becomes less useful, and optimal transport is obtained at a lower dephasing rate.

4.3.5 Inhomogeneous Systems

We consider the case of inhomogeneous transport by examining the FMO complex with systematically modified coupling strengthes between sites as described in Section 4.2.3. The site energies in an FMO model are inhomogeneous because they represent chromophores

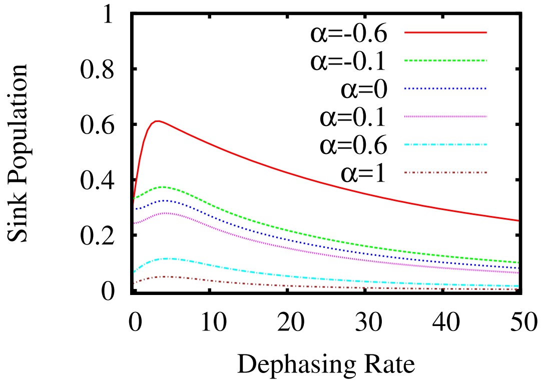

Figure 4.5: The sink population after 1 ps of the inhomogeneous FMO complex with optimal dephasing is reported as a function of a parameter α controlling the coupling strengths (the off-diagonal elements of the FMO Hamiltonian are multiplied by $e^{-\alpha}$). While the sink population decreases with decreasing coupling strength as in the homogeneous case, we observe, in contrast to the homogeneous case, that the optimal dephasing rate remains *essentially constant* with respect to changes in the coupling strength between sites.

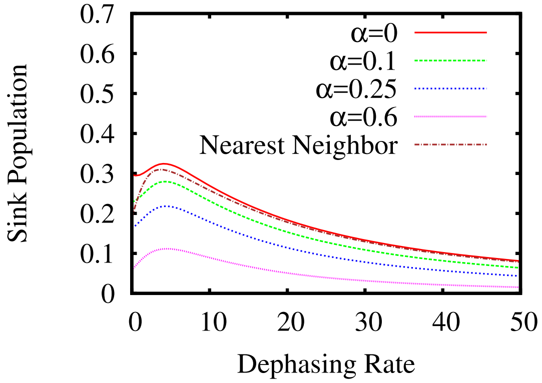

Figure 4.6: The sink population after 1 ps of the linearized FMO complex with optimal dephasing is reported as a function of a parameter α. For comparison we also present the results from a linearized FMO complex in which only nearest neighbor interactions are retained. As with the nonlinear topology in Fig. 4.5, we observe that the optimal dephasing rate remains essentially constant with changes in the coupling strength.

Table 4.4: To separate the inhomogeneity of the FMO site energies from the inhomogeneity of the FMO coupling energies, we examine two additional cases: (*i*) replacing the diagonal elements of the FMO Hamiltonian with a constant (homogeneous) value and varying the off-diagonal elements by $e^{-\alpha}$, and (*ii*) retaining the inhomogeneous FMO site energies and replacing the off-diagonal elements by those from homogeneous Hamiltonian in Eq. (4.1) with $A = 100$ a.u. If there exists a degree of homogeneity in either the site energies or the coupling energies, the optimal dephasing rate will increase with increasing coupling strength. However, between the two factors, we find that inhomogeneity in the coupling strengths is a more significant factor in setting a uniform dephasing rate than inhomogeneity in the site energies.

	Variations on FMO Complex			
α	Dephasing Rate	Sink Populations	Dephasing Rate	Sink Population
-0.6	3.40	0.579		
-0.1	2.10	0.455		
0	1.90	0.429	25	0.632
0.1	1.70	0.403	20	0.595
0.25	1.40	0.364	13	0.549
0.6	0.90	0.277	6	0.483
1	0.45	0.192	4	0.322

in different protein environments. In all calculations we initialize the exciton in site 1. In Fig. 4.5 we show the sink population of the FMO complex with optimal dephasing after 1 ps as a function of a parameter α controlling the coupling strengths (the off-diagonal elements of the FMO Hamiltonian are multiplied by $e^{-\alpha}$). Note that by definition the coupling strengths decrease with increasing α. While the sink population decreases with decreasing coupling strength as in the homogeneous case, we observe, in contrast to the homogeneous case, that the optimal dephasing rate remains *essentially constant* with respect to changes in the coupling strength between sites. Similar results were also obtained with several classes of randomly generated Hamiltonians with inhomogeneous site energies; because the trends were identical to those from the FMO-complex model in all cases, these results are not reported here. We emphasize that the high dephasing rate limit is not meant to represent an actual physical possibility for the FMO complex, but rather to demonstrate, as with the randomly generated Hamiltonians, a principle applicable to generalized inhomogeneous systems.

To ensure that these results were not due to the network topology in the FMO complex, we linearized the 7 sites of the FMO complex into a chain from site 1 through site 7 with the off-diagonal coupling elements of the Hamiltonian were multiplied by $e^{-\alpha\delta}$ (where $\delta = ||i - j||_2$). In Fig. 4.6 we present the sink population of the linearized FMO complex with optimal dephasing after 1 ps as a function of a parameter α. For comparison we also present the results from a linearized FMO complex in which only nearest neighbor interactions are retained. As with the nonlinear topology, we observe that the optimal dephasing rate remains essentially constant with changes in the coupling strength. The results from Fig. 4.5 and Fig. 4.6 are also summarized in Table 4.3.

To separate the inhomogeneity of the FMO site energies from the inhomogeneity of the FMO coupling energies, we examine two additional cases: (*i*) replacing the diagonal elements of the FMO Hamiltonian with a constant (homogeneous) value and varying the off-diagonal elements by $e^{-\alpha}$, and (*ii*) retaining the inhomogeneous FMO site energies and replacing the off-diagonal elements by those from homogeneous Hamiltonian in Eq. (4.1) with $A = 100$ a.u. In case (*i*) the optimal dephasing rate decreases from 3.5 times the base rate at $\alpha = -0.6$ to 0.5 times the base rate at $\alpha = 1$. In case (*ii*) the optimal dephasing rate changes from 25 times the base rate at $\alpha = 0$ to 4 times the base rate at $\alpha = 1$. The results are summarized in Table 4.4. If there exists a degree of homogeneity in either the site energies or the coupling energies, the optimal dephasing rate will increase with increasing coupling strength. However, between the two factors, we find that inhomogeneity in the coupling strengths is a more significant factor in setting a uniform dephasing rate than inhomogeneity in the site energies.

We can explain the relative invariance of the optimal dephasing with changes in coupling strength in inhomogeneous systems in terms of the local-modes picture. In the homogeneous system the dephasing is necessary to prevent the quantum system from becoming stuck in local coherent modes. As the degree of coupling between sites increases in the homogeneous system, the degree of environmental noise (dephasing) required for overcoming local modes also increases. In an inhomogeneous system, however, the inhomogeneity of the site and coupling energies function as a form of noise or disorder that is intrinsic to the quantum system which prevents the system from becoming trapped in local coherent modes. Consequently, we observe in inhomogeneous systems like the FMO complex that the optimal dephasing rate is relatively independent of a re-scaling of the coupling energy. To fully realize this effect, it is necessary for the system to be inhomogeneous in both the site energies and the coupling energies. Thus, we only find a nearly constant value for the optimal dephasing rate in Table 4.3.

4.3.6 Entanglement Between Sites and Dynamics

A natural question is whether entanglement between sites is integral to exciton transport, or merely a secondary effect of other factors. [47] write that entanglement decreases with increasing dephasing noise, a finding consistent with ours. We posit that local-mode entanglement (entanglement primarily between two sites) is a form of localization that can be detrimental to system transport.

In accordance with earlier research [57] we employ the squared Frobenius norm as the measure of entanglement. We use the square of the Frobenius norm instead of the norm itself as it is size extensive, *i.e.* it scales linearly with system size. Mathematical justification of this metric has been discussed in previous works [61, 36], in particular in [62] and [46]. We separately repeated the simulations using the definition of entanglement given by [52]. The results in both cases were found to be essentially identical, and as such only the results of the (squared) Frobenius norm are included.

We find that entanglement is not altogether detrimental. As shown in sections 4.3.1, 4.3.2, and 4.3.3, for all cases the optimal dephasing rate remains finite, and increasing the rate beyond this maximum is detrimental to transport, despite the fact that it will continue to reduce entanglement. Rather, we find that the optimal dephasing rate is enough to keep the degree of entanglement low but non-zero, as demonstrated for a linear homogeneous chain in Fig. 4.7. We note that this finding is consistent with the findings of [9] (in reference to

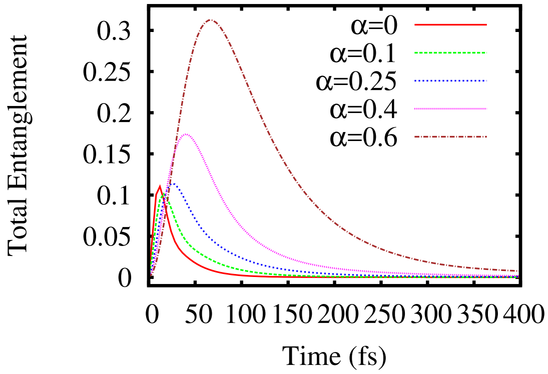

Figure 4.7: For a linear homogenous 9-site chain the total entanglement of the density matrix (defined as the sum of the squares of the off diagonals in the site basis) is given as a function of time where for each coupling parameter α the dephasing rate a was set to its optimal value. As the coupling strength decreases, the total entanglement decreases.

the FMO complex) that optimal transport efficiency is only obtained through an interplay of both entanglement and dephasing noise.

Our results are highly consistent with the results reported in Ref. [24] for a similar case, albeit without a sink. There it is reported that in the zero dephasing[3] limit, the system will display Anderson localization with sharp oscillations in site population. Eventually, the system will reach the limit of $D_{N,N} \sim e^{-cN}$ for each element of the density matrix D, where c is some constant.

However, if even slight dephasing is introduced, Anderson localization will be destroyed and the system will (without a sink to bias the flow) reach the limit of $D_{N,N} = 1/N$ for all sites in the matrix [24]. In our case, continuous siphoning by the sink prevents the system from reaching the equilibrium value of $1/N$. Thus the system keeps readjusting toward equilibrium of $1/N$ while N is reduced by exciton density draining into the sink.

In Fig. 4.7, when the dephasing rate is set to optimal, we find similar behavior across a range of coupling strengths α. Namely, after a period in which the entanglement spikes, it levels to a minimal but non-zero value. This is consistent with our claim in section 4.3.2,

---

[3] In Gurvitz's paper, what we refer to here as dephasing is referred to as decoherence.

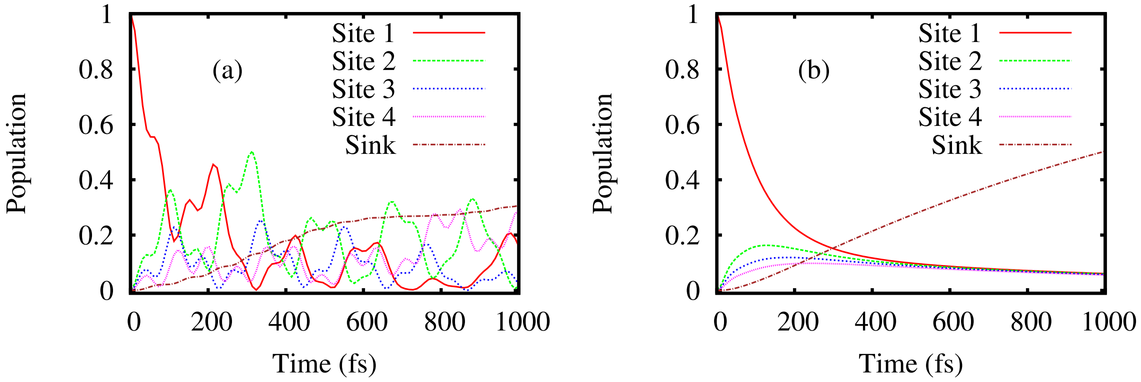

Figure 4.8: The exciton populations for a homogeneous chain of nine sites with the sink attached to the middle site and $\alpha = 0.25$ are given as functions of time. The figures show the site populations for the first four sites and the sink (a) without dephasing and (b) with the optimal dephasing rate of 10 times the FMO rate. The dephasing removes the oscillations in the populations arising from local modes that can limit the efficiency of the exciton transfer.

that the effect of dephasing is to collapse the local mode entanglement as it is formed, creating non-local transport throughout the system. At optimal dephasing, the exciton travels through the off-diagonal entangled states, but does not remain in them.

The optimal dephasing rate is closely related to oscillatory transport between sites, as demonstrated here and in [24]. The population of the nine sites of a linear chain with $\alpha = 0.25$ and the sink attached to the middle site is displayed in Fig. 4.8. When the dephasing rate was set below the optimal value of **10**, the transport between sites exhibited notable oscillations. It is found that at the optimal dephasing rate, these oscillations die off. Further increasing the dephasing rate (not shown) will continue to result in smooth, non-oscillatory transport, but will decrease the sink population. Although not shown here, the above trend was found to hold across a range of α values and connectivities in both homogeneous and inhomogeneous systems.

In a similar vein, we find that in cases of weak homogeneous coupling, local-mode entanglement will not form to any major extent. As such, there is no need for dephasing noise to damp the system's oscillations, and dephasing will be purely detrimental. For example, we previously mentioned in section 4.3.2 that for end-to-middle transport in a linear homo-

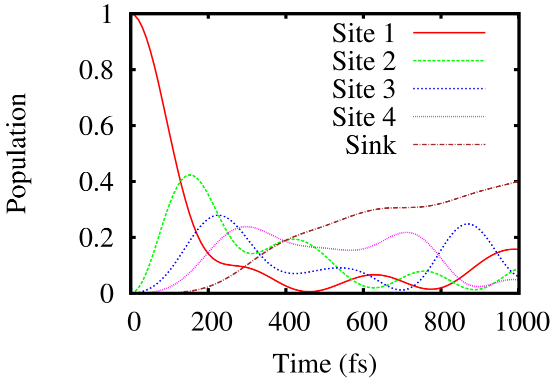

Figure 4.9: The exciton populations for end-to-middle transport in a linear homogeneous chain with $\alpha = 1$ and $a = 0$ are given as functions of time. Because the coupling strength is low, the oscillations are quite mild, corresponding to minimal local-mode entanglement even in the absence of dephasing ($a = 0$).

geneous chain, dephasing will no longer be beneficial for $\alpha \gtrsim 0.85$. In Fig. 4.9, we show the dynamics for end-to-middle transport in a linear homogeneous chain with $\alpha = 1$ and no dephasing. As can be seen, the oscillations are quite mild, corresponding to minimal local-mode entanglement even in the absence of dephasing.

We explain this behavior with a heuristic "damped oscillator" model, with dephasing serving as the damping parameter. When dephasing is set too low, there will exist a substantial exciton population in the local bipartite modes which will manifest as flopping between sites. When the system achieves optimal–or critical–damping, the off-diagonal population is kept low by forcing any bipartite states to collapse, allowing the exciton population to diffuse smoothly to the sink. Note that this is in line with the findings reported in Ref. [55] that, in the low dephasing limit, dephasing will work to force the exciton along the diagonal elements of the density matrix. Any further increase in dephasing rate will too significantly suppress the exciton's ability to utilize the non-local modes, effectively removing a means of transport from the system.

4.4 Discussion and Conclusions

We have examined excitonic transport for both one- and two-dimensional homogeneous and inhomogeneous quantum systems. Previous research has been expanded to a two-dimensional fully coupled topology of chromophore molecules. We find that in systems with a high degree of homogeneity that *the optimal dephasing rate increases monotonically as coupling strength increases, while in inhomogeneous systems the optimal dephasing rate is set by the system connectivity and is largely independent of coupling strength.* Although dephasing can facilitate transport, the effect is most pronounced in homogeneous systems with significant coupling between the chromophores. For the case of a degenerate chain nine sites long, we found that dephasing no longer has any benefit once coupling is as low as $\alpha = 0.85$; this corresponds to a nearest neighbor coupling of 43% of the site energy, and coupling to sites distant by two (next nearest neighbor) with 18% of the site energy.

We present evidence that the primary function of dephasing noise is to destroy the local-mode entanglement which primarily manifests as oscillations between two sites and can be viewed as a form of Anderson localization [2, 48]. Once the local modes have been destroyed, the system utilizes non-local mode entanglement across the system, allowing smoother transport across the entire system. Dephasing can be viewed as arising from a friction-like parameter in a damped oscillator.

It emerges that dephasing noise does not facilitate energy transfer in weakly coupled homogeneous systems that do not exhibit substantial local-mode entanglement. By the same token, environmental noise becomes increasingly important for more strongly coupled homogeneous systems that possess strong local-mode entanglement. For this reason, in the low-noise limit stronger coupling can paradoxically limit transport efficiency.

We have further demonstrated that highly inhomogeneous systems can partially defeat local-mode entanglement as a result of their network connectivity. The network connectivity largely establishes the optimal dephasing rate, which is therefore fairly constant with respect to re-scaling of the coupling strength. Although ultimately inhomogeneity is required in both the sites and the coupling energies to realize this effect, inhomogeneity in the coupling energies is the more significant factor. This is in sharp contrast to highly homogeneous systems, where the degree of local-mode entanglement, and hence the dephasing rate necessary to defeat it, is almost exclusively a function of the coupling strength. The above was found to hold true both the FMO complex Hamiltonian and several randomly generated Hamiltonians, and we predict that our findings will hold true across a wide range of inhomogeneous systems.

In this chapter we have described systems under study using the Lindblad formalism. The Lindblad equation is the most general form of a Markovian master equation which still preserves the positive semidefiniteness of the density matrix, unlike other master equations such as the Redfield equation. In situations where the Lindblad operators have a well-defined physical interpretation, as in Eqs. (4.4)-(4.6), the Lindblad is a suitable master equation. The relationship between optimal dephasing and coupling strength in homogeneous systems is dependent on the specific form of the Lindblad operator. Therefore, the results reported here depend not only upon the homogeneity of the site and coupling energies but also upon the physical form of the Lindblad operator.

The Lindblad equation will not describe non-Markovian effects. A natural extension of our research is to include non-Markovian bath effects in our models. In previous studies of the FMO complex there was found to exist a high degree of overall agreement between Markovian models and non-Markovian models such as in hierarchical equation-of-motion models [64, 28]. Similarly, results can depend on exciton-phonon interactions. Although we have not considered explicit phonon-modes in this work, previous studies [8, 9] indicate that such treatment would not change the fundamental results presented in this chapter. As such, although inclusion of phonon-modes and non-Markovian bath effects may yield important refinements to our findings, we believe that the results of such studies will be in general agreement with our findings.

In addition to its role in the context of photosynthetic light harvesting [48, 30, 43, 47, 19, 41], environmental noise has also been examined in the context of molecular quantum control [55]. Environmental noise can cooperate with a control field to drive a system and thereby lower the required control input to reach a given target. Indeed, when properly utilized, noise can behave as a form of quantum control, promoting desired transitions by suppressing undesired channels. It was observed in Ref. [55] that, when the control suppression is too high, it interferes with all channels including those that are desired. The present results may therefore be applicable to not only increasing the efficiency of excitonic transport in synthetic light harvesting systems but also better understanding systems in quantum information and quantum control.

Our findings may be of significance in guiding the design of a number of novel materials. In particular, recent advances in the fabrication of quantum dot photovoltaic devices have created arrays of quantum dots that primarily transfer energy through nonradiative dipole-dipole coupling [10]. Additionally, single-wall carbon nanotubes (SWCN) can be arranged to allow excitonic transport between units in a manner similar to that described by the model presented in this chapter [63, 4, 23].

REFERENCES

[1] Julia Adolphs and Thomas Renger. How proteins trigger excitation energy transfer in the fmo complex of green sulfur bacteria. *Biophys. J* ., 91(8):2778 – 2797, 2006.

[2] P. W. Anderson. Absence of diffusion in certain random lattices. *Phys. Rev.*, 109:1492–1505, Mar 1958.

[3] Daniela Ascenzi, Jana Roithová, Detlef Schröder, Emilie-Laure Zins, and Christian Alcaraz. Growth of doubly ionized c,h,n compounds in the presence of methane. *J. Phys. Chem. A*, 113(42):11204–11210, 2009.

[4] Dominick J. Bindl, Meng-Yin Wu, Frederick C. Prehn, and Michael S. Arnold. Efficiently harvesting excitons from electronic type-controlled semiconducting carbon nanotube films. *Nano Letters*, 11(2):455–460, 2011.

[5] M. Born and R. Oppenheimer. Zur quantentheorie der molekeln. *Annalen der Physik*, 389(20):457–484, 1927.

[6] A. Bouferguene, M. Fares, and P. E. Hoggan. Stop: A slater-type orbital package for molecular electronic structure determination. *Int. J. Quantum Chem.*, 57(4):801–810, 1996.

[7] S. F. Boys. Electronic Wave Functions. i. a General Method of Calculation for the Stationary States of Any Molecular System. *Proc. Roy. Soc. London Ser. A*, 200(1063):542–554, 1950.

[8] F. Caruso, A. W. Chin, A. Datta, S. F. Huelga, and M. B. Plenio. Highly efficient energy excitation transfer in light-harvesting complexes: The fundamental role of noise-assisted transport. *J. Chem. Phys.*, 131(10), 2009.

[9] Filippo Caruso, Susana F. Huelga, and Martin B. Plenio. Noise-enhanced classical and quantum capacities in communication networks. *Phys. Rev. Lett.*, 105:190501, Nov 2010.

[10] S. Chanyawadee, R. T. Harley, M. Henini, D. V. Talapin, and P. G. Lagoudakis. Photocurrent enhancement in hybrid nanocrystal quantum-dot *p-i-n* photovoltaic devices. *Phys. Rev. Lett.*, 102:077402, Feb 2009.

[11] Ilaria Ciofini, Philippe P. Lainé, and Carlo Adamo. Quantifying electron delocalization in orthogonal channels: Theoretical investigation of σ and π aromaticity in $\mathbf{C_6I_6^{2+}}$ and $\mathbf{C_6Cl_6^{2+}}$. *Chem. Phys. Lett.*, 435(46):171 – 175, 2007.

[12] Seth Coe, Wing-Keung Woo, Moungi Bawendi, and Vladimir Bulović. Electroluminescence from single monolayers of nanocrystals in molecular organic devices. *Nature*, 420(6917):800, 2002.

[13] A. J. Coleman. Structure of fermion density matrices. *Rev. Mod. Phys.*, 35:668–686, Jul 1963.

[14] Elisabetta Collini, Cathy Y. Wong, Krystyna E. Wilk, Paul M. G. Curmi, Paul Brumer, and Gregory D. Scholes. Coherently wired light-harvesting in photosynthetic marine algae at ambient temperature. *Nature*, 463(7281):644 – 647, 2010.

[15] A. Eugene DePrince and David A. Mazziotti. Parametric approach to variational two-electron reduced-density-matrix theory. *Phys. Rev. A*, 76:042501, Oct 2007.

[16] P. A. M. Dirac. Quantum mechanics of many-electron systems. *P. R. Soc. of Lond. A-Conta.*, 123(792):714–733, 1929.

[17] John H.D. Eland. Spectra of the dications of benzene, naphthalene and azulene. *Chem. Phys.*, 345(1):82 – 86, 2008.

[18] Gregory S. Engel, Tessa R. Calhoun, Elizabeth L. Read, Tae-Kyu Ahn, Tomas Mancal, Yuan-Chung Cheng, Robert E. Blankenship, and Graham R. Fleming. Evidence for wavelike energy transfer through quantum coherence in photosynthetic systems. *Nature*, 446:782–786, 2007.

[19] Kevin M. Gaab and Christopher J. Bardeen. The effects of connectivity, coherence, and trapping on energy transfer in simple light-harvesting systems studied using the haken-strobl model with diagonal disorder. *J. Chem. Phys.*, 121(16):7813–7820, 2004.

[20] Peter M. W. Gill, Andrew T. B. Gilbert, and Terry R. Adams. Rapid Evaluation of Two-Center Two-Electron Integrals. *J. Comput. Chem.*, 21(16):1505–1510, 2000.

[21] Peter M. W. Gill, Benny G. Johnson, and John A. Pople. Two-Electron Repulsion Integrals over Gaussian s Functions. *Int. J. Quantum Chem.*, 40(6):745–752, 1991.

[22] Peter M.W. Gill. Molecular Integrals over Gaussian Basis Functions. volume 25 of *Advances in Quantum Chemistry*, pages 141 – 205. Academic Press, 1994.

[23] Maksim Grechko, Yumin Ye, Randy D. Mehlenbacher, Thomas J. McDonough, Meng-Yin Wu, Robert M. Jacobberger, Michael S. Arnold, and Martin T. Zanni. Diffusion-assisted photoexcitation transfer in coupled semiconducting carbon nanotube thin films. *ACS Nano*, 8(6):5383–5394, 2014.

[24] S. A. Gurvitz. Delocalization in the anderson model due to a local measurement. *Phys. Rev. Lett.*, 85:812–815, Jul 2000.

[25] Miho Hatanaka, Masaichi Saito, Masahiro Fujita, and Keiji Morokuma. σ-aromaticity in hexa-group 16 atom-substituted benzene dications: A theoretical study. *J. Org. Chem.*, 79(6):2640–2646, 2014.

[26] Martin Head-Gordon and John A. Pople. A Method for Two Electron Gaussian Integral and Integral Derivative Evaluation using Recurrence Relations. *J. Chem. Phys.*, 89(9):5777–5786, 1988.

[27] Trygve Helgaker, Poul Jørgensen, and Jeppe Olsen. *Molecular Electronic-Structure Theory.* Wiley, 2000.

[28] Akihito Ishizaki and Graham R. Fleming. Theoretical examination of quantum coherence in a photosynthetic system at physiological temperature. *Proc. Natl. Acad. Sci. U.S.A.*, 113:17255–17260, 2009.

[29] Juraj Jašík, Dieter Gerlich, and Jana Roithová. Probing isomers of the benzene dication in a low-temperature trap. *J. Am. Chem. Soc.*, 136(8):2960–2962, 2014.

[30] Ivan Kassal and Alán Aspuru-Guzik. Environment-assisted quantum transport in ordered systems. *New J. Phys.*, 14(053041), 2012.

[31] Monther A. Khanfar and Konrad Seppelt. Fluorinated benzene cations. *J. Fluorine Chem.*, 179:193 – 197, 2015.

[32] Karsten Krogh-Jespersen. Ab initio electronic structure calculations on the benzene dication and other $\mathbf{C_6H_6^{2+}}$ isomers. *J. Am. Chem. Soc.*, 113(2):417–423, 1991.

[33] Kyle M. Lancaster, Michael Roemelt, Patrick Ettenhuber, Yilin Hu, Markus W. Ribbe, Frank Neese, Uwe Bergmann, and Serena DeBeer. X-ray emission spectroscopy evidences a central carbon in the nitrogenase iron-molybdenum cofactor. *Science*, 334(6058):974–977, 2011.

[34] G. Lindblad. On the generators of quantum dynamical semigroups. *Commun. Math. Phys.*, 48:119, 1976.

[35] Wenlan Liu, Volker Settels, Philipp H. P. Harbach, Andreas Dreuw, Reinhold F. Fink, and Bernd Engels. Assessment of td-dft- and td-hf-based approaches for the prediction of exciton coupling parameters, potential energy curves, and electronic characters of electronically excited aggregates. *J. Comput. Chem.*, 32(9):1971 – 1981, 2011.

[36] Robert B. Lockhart and Michael J. Steiner. Preserving entanglement under perturbation and sandwiching all separable states. *Phys. Rev. A*, 65:022107, Jan 2002.

[37] Moritz Malischewski and K. Seppelt. Crystal structure determination of the pentagonal-pyramidal hexamethylbenzene dication $\mathbf{C_6(CH_3)_6^{2+}}$. *Angew. Chem. Int. Edit.*, 56(1):368–370, 2017.

[38] David A. Mazziotti. Quantum chemistry without wave functions: two-electron reduced density matrices. *Acc. Chem. Res.*, 39(3):207–215, 2006.

[39] David A. Mazziotti. Effect of strong electron correlation on the efficiency of photosynthetic light harvesting. *J. Chem. Phys.*, 137(7), 2012.

[40] David A. Mazziotti and Robert M. Erdahl. Uncertainty relations and reduced density matrices: Mapping many-body quantum mechanics onto four particles. *Phys. Rev. A*, 63:042113, Mar 2001.

[41] J. J. Mendoza-Arenas, T. Grujic, D. Jaksch, and S. R. Clark. Dephasing enhanced transport in nonequilibrium strongly correlated quantum systems. *Phys. Rev. B*, 87:235130, Jun 2013.

[42] M. Mohseni, A. Shabani, S. Lloyd, Y. Omar, and H. Rabitz. Geometrical effects on energy transfer in disordered open quantum systems. *J. Chem. Phys.*, 138(20), 2013.

[43] Masoud Mohseni, Patrick Rebentrost, Seth Lloyd, and Alán Aspuru-Guzik. Environment-assisted quantum walks in photosynthetic energy transfer. *J. Chem. Phys.*, 129(17), 2008.

[44] S. Obara and A. Saika. Efficient Recursive Computation of Molecular Integrals over Cartesian Gaussian Functions. *J. Chem. Phys.*, 84(7):3963–3974, 1986.

[45] Philip Pearle. Simple derivation of the lindblad equation. *Eur. J. Phys.*, 33(4):805, 2012.

[46] Arthur O. Pittenger and Morton H. Rubin. Convexity and the separability problem of quantum mechanical density matrices. *Linear Algebra Appl.*, 346(13):47 – 71, 2002.

[47] Martin B. Plenio and Susana F. Huelga. Dephasing-assisted transport: quantum networks and biomolecules. *New J. Phys.*, 10(113019), 2008.

[48] Patrick Rebentrost, Masoud Mohseni, Ivan Kassal, Seth Lloyd, and Alán Aspuru-Guzik. Environment-assisted quantum transport. *New J. Phys.*, 11(3):033003, 2009.

[49] Simen Reine, Erik Tellgren, and Trygve Helgaker. A Unified Scheme for the Calculation of Differentiated and Undifferentiated Molecular Integrals over Solid-Harmonic Gaussians. *Phys. Chem. Chem. Phys.*, 9:4771–4779, 2007.

[50] D. J. Sagl and J. C. Martin. The stable singlet ground state dication of hexaiodobenzene: possibly a σ-delocalized dication. *J. Am. Chem. Soc.*, 110(17):5827–5833, 1988.

[51] Andrew M. Sand, Claire Liu, Andrew J. S. Valentine, and David A. Mazziotti. Modulating the electronic structure of chromophores by chemical substituents for efficient energy transfer: Application to fluorone. *J. Phys. Chem. A*, 118(31):6085–6091, 2014.

[52] Mohan Sarovar, Akihito Ishizaki, Graham R. Fleming, and K. Birgitta Whaley. Quantum entanglement in photosynthetic light-harvesting complexes. *Nat. Phys.*, 6:462–467, 2010.

[53] H. Bernhard Schlegel. An Efficient Algorithm for Calculating *ab initio* Energy Gradients using s, p Cartesian Gaussians. *J. Chem. Phys.*, 77(7):3676–3681, 1982.

[54] H. Bernhard Schlegel and Michael J. Frisch. Transformation between Cartesian and Pure Spherical Harmonic Gaussians. *Int. J. Quantum Chem.*, 54(2):83–87, 1995.

[55] Feng Shuang and Herschel Rabitz. Cooperating or fighting with decoherence in the optimal control of quantum dynamics. *J. Chem. Phys.*, 124(15), 2006.

[56] Nolan Skochdopole and David A. Mazziotti. Functional subsystems and quantum redundancy in photosynthetic light harvesting. *J. Phys. Chem. Lett.*, 2(23):2989–2993, 2011.

[57] Julie T. Skolnik and David A. Mazziotti. Cumulant reduced density matrices as measures of statistical dependence and entanglement between electronic quantum domains with application to photosynthetic light harvesting. *Phys. Rev. A*, 88:032517, Sep 2013.

[58] Attila Szabo and Neil S. Ostlund. *Modern quantum chemistry: introduction to advanced electronic structure theory.* Dover Publications, Mineola, N.Y., 1996. Previously published: 1st ed., rev. New York : McGraw-Hill, c1989.

[59] Dmitri V. Talapin, Jong-Soo Lee, Maksym V. Kovalenko, and Elena V. Shevchenko. Prospects of colloidal nanocrystals for electronic and optoelectronic applications. *Chem. Rev.*, 110(1):389–458, 2010.

[60] R. H. Tredgold. Density matrix and the many-body problem. *Phys. Rev.*, 105:1421–1423, Mar 1957.

[61] V. Vedral and M. B. Plenio. Entanglement measures and purification procedures. *Phys. Rev. A*, 57:1619–1633, Mar 1998.

[62] C. Witte and M. Trucks. A new entanglement measure induced by the hilbertschmidt norm. *Phys. Lett. A*, 257(12):14 – 20, 1999.

[63] Cathy Y. Wong, Carles Curutchet, Sergei Tretiak, and Gregory D. Scholes. Ideal dipole approximation fails to predict electronic coupling and energy transfer between semiconducting single-wall carbon nanotubes. *J. Chem. Phys.*, 130(8), 2009.

[64] Jing Zhu, Sabre Kais, Patrick Rebentrost, and Alan Aspuru-Guzik. Modified scaled hierarchical equation of motion approach for the study of quantum coherence in photosynthetic complexes. *J. Phys. Chem. B*, 115(6):1531–1537, 2011.